

Learning to Drive in New Cities Without Human Demonstrations

Zilin Wang^{† 1 2} Saeed Rahmani^{† 1 3} Daphne Cornelisse⁴ Bidipta Sarkar^{1 2} Alexander David Goldie^{1 2}
 Jakob Nicolaus Foerster^{‡ 2} Shimon Whiteson^{‡ 1}

Abstract

While autonomous vehicles have achieved reliable performance within specific operating regions, their deployment to new cities remains costly and slow. A key bottleneck is the need to collect many human demonstration trajectories when adapting driving policies to new cities that differ from those seen in training in terms of road geometry, traffic rules, and interaction patterns. In this paper, we show that self-play multi-agent reinforcement learning can adapt a driving policy to a substantially different target city using only the map and meta-information, *without requiring any human demonstrations from that city*. We introduce **NO** data Map-based self-play for Autonomous Driving (NOMAD), which enables policy adaptation in a simulator constructed based on the target-city map. Using a simple reward function, NOMAD substantially improves both task success rate and trajectory realism in target cities, demonstrating an effective and scalable alternative to data-intensive city-transfer methods. Project Page: <https://nomaddrive.github.io/>

1. Introduction

Autonomous vehicles have improved dramatically over the past few years and now outperform humans in certain environments (Kusano et al., 2025; Di Lillo et al., 2024). However, they still operate reliably in only a small fraction of the global road network (Waymo, 2025b). For many current deployments, scaling and expansion remain a gradual, city-by-city effort (Waymo, 2025a). This is mainly because different cities, especially those in different countries or continents, vary in road geometry, traffic rules, and interaction patterns, i.e., the spatiotemporal behaviors induced by

[†]Core Contributor, [‡]Equal Supervision ¹WhiRL, University of Oxford ²FLAIR, University of Oxford ³Delft University of Technology ⁴NYU Tandon School of Engineering. Correspondence to: Zilin Wang <zilin.wang@lmh.ox.ac.uk>.

Preprint. February 19, 2026.

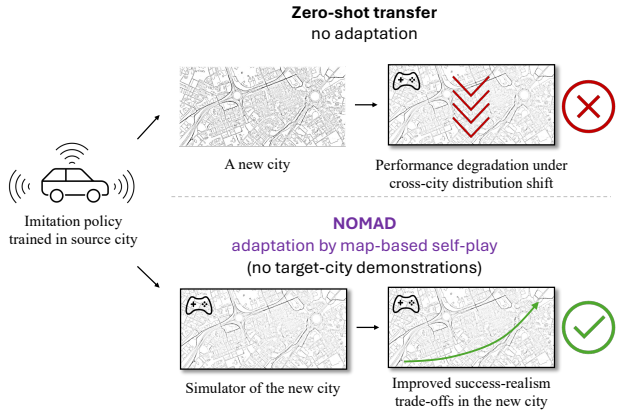


Figure 1. City transfer in autonomous driving. Top: Zero-shot deployment of an imitation policy trained in a source city into a new city leads to performance degradation due to cross-city distribution shift. Bottom: NOMAD adapts the same policy to the target city using only the target-city map and easily accessible meta-information, *without any human demonstrations*, by performing map-based self-play multi-agent reinforcement learning in a simulator of the new city. This adaptation substantially improves the policy’s success rate and realism in the new city.

road topology, intersection design, and traffic density (Sun et al., 2023; Li et al., 2024a; Vasudevan et al., 2025). As a result, models trained with imitation learning in one city may exhibit degraded performance when deployed elsewhere (Feng et al., 2024), leading to passenger discomfort or even unsafe driving (Yasarla et al., 2025).

Current deployment pipelines address this problem by collecting new human demonstrations in target cities and fine-tuning policies on the new data (Leussink & Freed, 2025). However, this approach is slow and expensive, and hinders rapid expansion. If human demonstrations were not needed for geographic expansion, we could substantially reduce both the cost and the time needed to deploy autonomous vehicles at scale. This motivates a fundamental question:

Can we adapt driving policies to new cities without collecting additional human demonstrations from them?

Fortunately, although collecting driving trajectories in new cities is resource intensive, other forms of city information are more readily accessible. In particular, the lane-level

map and traffic meta-information, such as speed limits and traffic density, are prevalent and inexpensive.

Motivated by this observation, we introduce **NO** data **M**ap-based self-play for **A**utonomous **D**riving (NOMAD). As illustrated in Figure 1, NOMAD first constructs a simulator of the target city using its lane-level map and readily available traffic meta-information, such as speed limits and traffic density. This design is motivated by the hypothesis that much of the disparity in optimal driving behavior across cities is determined at the map level. A policy trained via imitation learning in the source city is then adapted through self-play multi-agent reinforcement learning (*self-play MARL*) within this simulator. During self-play, the policy interacts with other agents and explores feasible maneuvers and interaction dynamics induced by the target-city map, thereby acquiring experience that effectively substitutes for target-city demonstrations. Importantly, the adaptation relies on a *simple reward function*, avoiding city-specific reward engineering or manual tuning. We achieve it by anchoring the adaptation to the source-city policy via KL regularization, which preserves the behavioral prior learned from real human driving data in the source city while allowing deviations only where required by the target-city map and interaction structure. This selective adaptation substantially improves both success rate and behavioral realism in the target city.

Extensive closed-loop experiments demonstrate that NOMAD substantially improves zero-shot policy performance in unseen cities without relying on target-city human trajectories or complex reward engineering. In the Boston-to-Singapore transfer setting, NOMAD increases the success rate from 42% under zero-shot transfer to over 90%, while simultaneously improving trajectory realism from 0.679 to approximately 0.765, as measured by the WOSAC (Montali et al., 2023) realism metric in closed-loop evaluation. Furthermore, selected checkpoints produced by NOMAD form a Pareto frontier over success rate and realism, with each frontier checkpoint representing the best achievable policy for a particular success–realism trade-off. This enables practitioners to select deployment policies based on problem-specific requirements. We also conduct systematic analyzes of NOMAD, including the role of behavioral priors, the necessity of target-city map, comparison against policy with target-city demonstration access, generalization across diverse cities, and a sensitivity study on KL regularization strength. Overall, these results indicate that NOMAD substantially narrows cross-city generalization gaps, supporting scalable deployment of autonomous driving systems across diverse environments and highlighting the promise of self-play MARL for improving safety and robustness.

2. Related Work

2.1. Large-Scale Deployment of Autonomous Driving

Recent large-scale advances in autonomous driving have been driven by three complementary paradigms: the incorporation of Large Language/Vision-Language Models that leverage rich world knowledge to handle corner cases and improve generalization (Shao et al., 2024; Sima et al., 2024; Tian et al., 2024; Renz et al., 2025; Fu et al., 2025); World Models that act as data engines generating diverse traffic scenarios for training and evaluation (Hu et al., 2023; Russell et al., 2025; Ren et al., 2025; Wang et al., 2024); and simulation at scale providing infrastructure for closed-loop training and validation (Dosovitskiy et al., 2017; Montali et al., 2023; Caesar et al., 2021; Cao et al., 2025). However, a critical barrier remains: robustness under domain distribution shift. While early efforts addressed perception shifts across weather and sensor conditions (Sakaridis et al., 2018; Michaelis et al., 2019; Muhammad et al., 2022; Li et al., 2024b; Jeon et al., 2024), these scalable paradigms do not fully eliminate the need for explicit adaptation to new cities, where road geometry, traffic rules, and interaction patterns vary significantly—motivating the city-transfer setting discussed next.

2.2. City Transfer of Autonomous Driving

Transferring policies across diverse cities presents a more specific challenge. Vasudevan et al. (2025) demonstrate significant behavioral differences among different cities in the nuPlan dataset. UniTraj (Feng et al., 2024) shows that even state-of-the-art trajectory prediction models trained with large datasets struggle to generalize to new cities. Additionally, Yasarla et al. (2025) show that L2 error and collision rate both increase substantially when planners are transferred zero-shot to a new city.

These findings motivate the need for explicit cross-city adaptation mechanisms. TeraSim-World (Wang et al., 2025) proposes a pipeline to generate driving scenarios worldwide using the Cosmos-Drive world model (Ren et al., 2025). However, this approach still depends on world models that may not generate accurate scenarios for unseen cities. As an alternative, Vasudevan et al. (2025) propose AdaptiveDriver, a rule-based planner that adapts its behavior in new cities via interactions with a learned reactive world model. While their approach shows modest generalization to held-out cities within nuPlan, it still requires logged trajectories to calibrate the reactive world model in the new cities. Furthermore, the world model relies on IDM’s (Kesting et al., 2010) single-agent car-following formulation, which limits the planner’s ability to reason about complex multi-agent interactions. Moreover, RoCA (Yasarla et al., 2025) improves cross-domain robustness of end-to-end planners via a GP-based probabilistic to-

ken model and uncertainty-guided adaptation, achieved by prioritizing the most informative target data for finetuning. As another avenue to consider, LLaDA (Li et al., 2024a) uses Large Language Models to interpret text-based traffic codes and correct plan violations. While effective for explicit constraints like traffic rules, this approach struggles to capture geometry-dependent dynamics that are crucial for smooth trajectory planning but not formally codified in text. Although Wayve (2025) shows that large-scale foundation driving models can enable zero-shot transfer when the target city lies close enough to the training distribution, demonstration collection is necessary for cities with distinctly different traffic patterns. In contrast, NOMAD enables city transfer without collecting any logged trajectories from the target city. It adapts driving policies through experience gathered via self-play in simulator constructed from target-city map and meta-information, avoiding reliance on learned world models, target-city demonstrations, or industrial-scale training pipelines.

2.3. Self-Play for Autonomous Driving

Self-play is a powerful paradigm for training agents by allowing policies to improve through interactions with *copies of themselves*. CoPO (Peng et al., 2021) uses coordinated policy optimization to simulate self-driven particle systems in traffic by enabling agents to dynamically shift between cooperative and competitive behaviors. More recently, Cusumano-Towner et al. (2025) demonstrate that robust and naturalistic driving can emerge from self-play. A key challenge in self-play for driving, however, is maintaining human-like behavior while optimizing for task completion. Cornelisse & Vinitsky (2024) address this by regularizing self-play against a human reference policy. They also show that scaling self-play across thousands of Waymo scenarios yields reliable agents with over 99% goal completion and minimal collisions (Cornelisse et al., 2025). Similarly, SPACER (Chang et al., 2025) introduces a self-play framework that stabilizes RL training by anchoring decentralized agents to a centralized reference policy, mitigating non-stationarity while enabling human-like behavior learning. Beyond trajectory planning, self-play has been applied to asymmetric scenario generation (Zhang et al., 2024), where a teacher policy learns to create challenging yet solvable scenarios for a student, and to natural language communication for cooperative driving (Cui et al., 2025). While prior self-play methods target robustness and realism within a single domain, NOMAD repurposes self-play for cross-city transfer. By conducting self-play in map-based simulators of the target city, NOMAD enables adaptation without any target-city demonstrations.

3. Preliminaries and Problem Formulation

We model a target city C as a distribution over its map and traffic scenarios, $C = (\mathcal{M}_C, \Xi_C)$. Specifically, we sample a map segment $m \sim \mathcal{M}_C$, namely road layout and traffic direction, from a given region of the target city. Conditioned on m , we then sample a scenario $\xi = (s_0, \{g^i\}_{i=0}^{N-1}, m) \sim \Xi_C(\cdot|m)$, which specifies number of agents N , the initial state s_0 , goal positions for all agents $\{g^i\}_{i=0}^{N-1}$, and the map segment m . Given a traffic scenario ξ , rolling out a policy π produces a trajectory $\tau \sim q_\pi(\cdot|\xi)$, where $q_\pi(\cdot|\xi)$ denotes the trajectory distribution induced by π in closed loop. We evaluate the performance of policy π with two metrics, success rate and realism, that are broadly accepted by the community (Li et al., 2022; Montali et al., 2023; Cornelisse* et al., 2025; Cusumano-Towner et al., 2025).

Success rate is the probability of a given vehicle reaching the goal-centered neighborhood within the horizon H :

$$\mathcal{S}(\pi, C) := \mathbb{E}_{\xi \sim \Xi_C} [\mathbb{E}_{\tau \sim q_\pi(\cdot|\xi)} [\mathbb{1}(\exists t \leq H : d(p_t, g) \leq \epsilon)]] , \quad (1)$$

where p_t and g are the ego position at time t and the goal position, respectively. $\mathbb{1}(\cdot)$ is the indicator function. And ϵ is the error tolerance in reaching the goal.

Realism measures how well generated trajectories match the actual distribution of real-world driving behavior. Because the true distribution of real-world driving is unknown, we estimate realism using the likelihood of logged human trajectories under the trajectory distribution induced by π . Formally, we define:

$$\mathcal{R}(\pi, C) := \mathbb{E}_{\xi \sim \Xi_C} [\mathbb{E}_{\tau \sim p(\cdot|\xi)} [\log q_\pi(\tau|\xi)]] , \quad (2)$$

where $p(\tau|\xi)$ denotes the distribution of logged human trajectories in the scenario ξ . Importantly, this realism metric requires access to target-city human trajectories *only for evaluation*. These trajectories are never used during training or adaptation, and serve solely as an offline benchmark for assessing behavior realism. Overall, we evaluate the policy π in city C by a multi-objective score

$$\mathbf{J}(\pi, C) = (\mathcal{S}(\pi, C), \mathcal{R}(\pi, C)). \quad (3)$$

City adaptation without demonstrations. Let π^0 be a planner trained using source-city data (e.g., via behavior cloning) and deployed zero-shot in target city C . Given target-city priors (the map \mathcal{M}_C and meta-information \mathcal{I}_C such as speed limits and traffic density), but no target-city demonstrations, our goal is to learn a *set* of adapted policies:

$$\Pi^+(C) = \text{Adapt}(\pi^0; \mathcal{M}_C, \mathcal{I}_C) = \{\pi^{+(1)}, \dots, \pi^{+(N)}\} \quad (4)$$

that offer improved success-realism trade-offs in the target city. Namely, $\Pi^+(C)$ should contain policies that Pareto-dominate the zero-shot baseline:

$$\exists \pi^+ \in \Pi^+(C) \text{ s.t. } \mathbf{J}(\pi^+, C) \succ \mathbf{J}(\pi^0, C), \quad (5)$$

where \succ indicates Pareto dominance. In practice, $\Pi^+(C)$ contains multiple candidate policies (e.g., checkpoints), from which we extract an empirical Pareto frontier. Ideally, we aim to expand the achievable Pareto frontier in the target city, yielding improved trade-offs across a wide range of success-realism preferences.

Deployment. At deployment time, a practitioner selects a single policy $\pi^{\text{deploy}} \in \Pi^+(C)$ according to application-specific preferences (e.g., prioritizing success rate or trajectory realism), corresponding to choosing an operating point along the induced Pareto frontier.

4. Multi-Agent Interaction Model

We formulate city adaptation problem as a partially observable stochastic game (POSG) (Hansen et al., 2004) defined by the tuple $(N, S, A, O, P, Z, r, H, \gamma, b_0)$, where each agent in the game is indexed by $i \in \{0, 1, \dots, N-1\}$, and S is the set of possible states. P is the state transition function, deciding the probability of the next state s_{t+1} via joint action a_t at the state s_t . For agent i , A^i and O^i are the set of possible actions and observations, respectively. $Z^i(o_t^i | s_t, a_t, s_{t+1})$ is the observation function. $r^i(s_t, a_t, s_{t+1})$ is the scalar reward function. γ is the discount factor and b_0 is the probability of initial state s_0 . We focus on homogeneous agents: all vehicles share the same observation space, action space, and reward function. This symmetry naturally supports a shared-parameter policy, which we exploit for scalable self-play training.

Observation space. At each timestep, each dynamic vehicle i receives a partial observation o_t^i consisting of its local ego state (e.g., velocity and goal) and a limited-range perception of nearby vehicles and road information (e.g., edges and lanes in a neighborhood). To facilitate learning and support parameter sharing, all observations are expressed in an ego-centric coordinate frame (Figure 7).

Action space. We adopt decentralized, memoryless policies $\pi(a_t^i | o_t^i)$, where temporal information such as velocity is encoded directly in the observation. At each step, the policy predicts discrete action increments in position and heading, $a_t^i = (\delta_x^i, \delta_y^i, \delta_h^i)$. These increments are defined in the ego vehicle's coordinate frame and are deterministically applied using kinematic pose updates. Each action dimension is bounded and uniformly discretized into multiple bins. A discretized action space improves training stability during reinforcement learning and supports multi-modal behavior naturally during imitation learning. In addition, it

respects vehicle motion constraints and is commonly used in trajectory prediction and planning tasks (Phlion et al., 2024; Cornelisse & Vinitsky, 2024; Wu et al., 2024; Zhang et al., 2025).

Reward function. Reward design in autonomous driving is non-trivial due to the difficulty of balancing safety, progress, and other factors (Knox et al., 2023). Moreover, precise reward engineering often requires substantial iterative tuning (Wurman et al., 2022) and can be brittle under transfer, since optimized policies may overfit to environment-specific reward proxies or simulator details, leading to degraded performance under distribution shift (Zhang et al., 2018; Pan et al., 2022). To demonstrate that NOMAD's effectiveness stems from the adaptation framework itself rather than reward tuning, we deliberately adopt a minimal reward formulation:

$$r^i(s_t, a_t, s_{t+1}) = w_g \mathbb{1}_{\mathcal{G}^i(s_{t+1})} + w_c \mathbb{1}_{\mathcal{C}^i(s_{t+1})} + w_o \mathbb{1}_{\mathcal{O}^i(s_{t+1})} \quad (6)$$

where $\mathbb{1}(\cdot)$ is the indicator function. $\mathcal{G}^i(s_t)$, $\mathcal{C}^i(s_t)$, and $\mathcal{O}^i(s_t)$ represent if the goal is reached, a collision occurs, and the car drives offroad for agent i at timestep t , respectively. w_g , w_c , and w_o are corresponding weights, set as 1.0, -0.75, and -0.75, respectively, in all experiments.

5. NOMAD

We now introduce **NO** data **M**ap-based self-play for **A**utonomous **D**riving (NOMAD), which leverages map-based simulation and self-play MARL to adapt a driving policy to a new city without target-city demonstrations.

5.1. Overview

Figure 2 provides an overview of NOMAD. Let C be the city we want to transfer to, assuming the target-city map \mathcal{M}_C and the city-specific meta-information \mathcal{I}_C are accessible. \mathcal{I}_C consists only of coarse information that is typically known a priori (e.g., speed limits and traffic density). Importantly, \mathcal{I}_C is *global* to the city, independent of the specific map segment m , and low-dimensional, and thus does not require any trajectory data or city-specific learning.

Based on this, we construct a scenario generator $\Xi_\varphi(\xi | m, \mathcal{I}_C)$ with a learned or heuristic generic parameter φ to approximate the true distribution of scenarios $\Xi_C(\xi | m)$ in city C . The generator is used only to sample initial agent states and goal locations; it does *not* generate expert trajectories, driving behaviors, or policies. Any method that samples initial states and goals from the map can be used, and NOMAD, which focuses on map-based self-play rather than scenario generation, is agnostic to the specific scenario generation procedure. The scenario generator used in our experiments is described in Appendix C. The generated scenarios $\xi = (s_0, \{g^i\}_{i=0}^{N-1}, m)$ are next

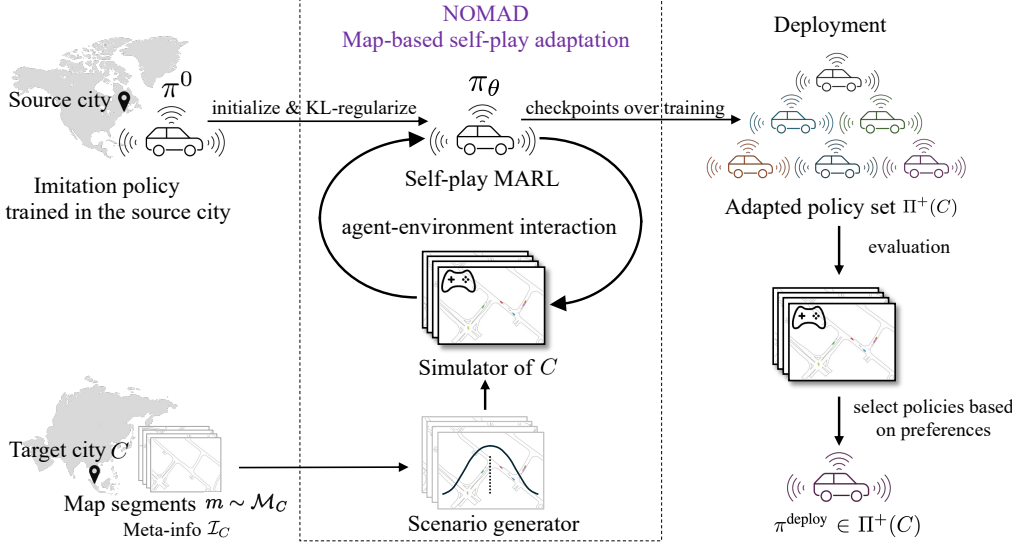


Figure 2. NOMAD overview. Starting from a source-city imitation policy π^0 , NOMAD adapts it to a target city C using map segments $m \sim \mathcal{M}_C$ and meta-information \mathcal{I}_C . A scenario generator samples initial states and goals that are loaded in a data-driven multi-agent simulator, yielding a simulator of C . The policy π_θ is initialized from π^0 and optimized via KL-regularized self-play MARL. Training checkpoints produce an adapted policy set $\Pi^+(C)$, from which a deployment policy π^{deploy} is chosen based on practitioner preferences.

loaded into a multi-agent data-driven autonomous driving simulator like GPUDrive (Kazemkhani et al., 2025), Waymax (Gulino et al., 2023), or Nocturne (Vinitsky et al., 2022), yielding a simulator of the target city C .

Starting from an imitation learning policy π^0 from the source city, we initialize a policy π_θ and adapt it to the target city through KL-regularized self-play within the simulator. Training produces a set of adapted policies $\Pi^+(C)$ that achieve Pareto improvements over the zero-shot policy π^0 . At deployment time, practitioners select a policy $\pi^{\text{deploy}} \in \Pi^+(C)$ along the induced Pareto frontier based on their preferences over success rate and realism.

5.2. Policy Adaptation via Regularized Self-Play

NOMAD solves the POSG described in Section 4 with regularized self-play. By requiring all agents to share a single policy $\pi_\theta(a_t|o_t)$ parameterized by θ , we can scale RL training to dense urban environments more effectively since the number of parameters is independent of the number of vehicles controlled. In addition, it also boosts training efficiency by allowing a single policy to learn from the diverse experiences collected by all agents simultaneously. We train π_θ with independent PPO (IPPO) due to its simplicity and efficacy (De Witt et al., 2020; Yu et al., 2022). IPPO treats each agent as an independent learner that optimizes a standard PPO objective,

$$\max_{\theta} J_{\text{PPO}}(\theta) = \mathbb{E}_{(o,a) \sim \pi_{\theta_{\text{old}}}} \left[\min \left(\frac{\pi_\theta(a|o)}{\pi_{\theta_{\text{old}}}(a|o)} A_{\pi_{\theta_{\text{old}}}}(o, a), \right. \right. \\ \left. \left. \text{clip} \left(\frac{\pi_\theta(a|o)}{\pi_{\theta_{\text{old}}}(a|o)}, 1 - \epsilon, 1 + \epsilon \right) A_{\pi_{\theta_{\text{old}}}}(o, a) \right) \right], \quad (7)$$

using its own local observations and rewards, modeling the other agents as part of a non-stationary environment.

Given our minimal reward formulation, optimization without regularization could yield policies that complete goals but deviate from human-like driving patterns. To retain useful knowledge from the source city and mitigate reward hacking, we regularize the learned policy toward the prior π^0 using reverse Kullback–Leibler divergence. This choice penalizes assigning probability mass to actions deemed unlikely by the prior, thereby discouraging unnatural driving while allowing selective adaptation when required by the target city. The regularized objective is:

$$\max_{\theta} J(\theta) = J_{\text{PPO}}(\theta) \\ - \lambda_{\text{KL}} \cdot \mathbb{E}_{\pi_\theta} \left[\frac{1}{H} \sum_{t=0}^{H-1} D_{\text{KL}}(\pi_\theta(\cdot|o_t) \parallel \pi^0(\cdot|o_t)) \right], \quad (8)$$

where D_{KL} is the KL divergence and λ_{KL} is a regularization weight, whose effects we analyze in Section 7.6.

6. Experimental Setup

Datasets and Simulator. We use nuPlan (Caesar et al., 2021), a large-scale dataset collected from the U.S. and Singapore. NuPlan stores the scenarios separately by cities and provides cross-continental coverage, which enables studying city transfer under large distribution shifts. For instance, Singapore and U.S. cities like Boston and Pittsburgh differ both in road topology and traffic handedness. In our experiments, we randomly select 4,000 traffic scenarios for each city, partitioned into 3,200 for training and 800 for test. For closed-loop traffic simulation, we use

GPUDrive (Kazemkhani et al., 2025), a GPU-accelerated data-driven simulation tool suitable for fast and efficient RL training. We converted the nuPlan dataset into the format supported by GPUDrive, with 9-second scenarios discretized at 10 Hz.

Scenario Generation. We use a heuristic scenario generator $\Xi_\varphi(\cdot|m, \mathcal{I}_C)$ conditioned on the map, speed limits, and traffic density to produce feasible and realistic spawn and goal points for self-play simulation in the target city. For each map segment, we generate $K = 8$ distinct scenarios, yielding a total of $3,200 \times 8 = 25,600$ unique traffic scenarios for training. Appendix C provides a detailed algorithm description and visualizations.

Metrics. Evaluation is based on two core metrics, *success rate* and *realism*, defined in Section 3. For realism, we adopt the Waymo Open Sim Agents Challenge (WOSAC) evaluation metric (Montali et al., 2023). WOSAC aggregates weighted components over kinematics (e.g., speed and acceleration), interaction features (e.g., time-to-collision and collisions), and map compliance (e.g., road departures). The detailed definitions and weights of each component, as well as motivation for choosing WOSAC evaluation metric over other metrics, are provided in Appendix E. We also report the results on each sub-metric, collision rate, offroad rate, and average displacement error (ADE) in Appendix F.

Training details and baselines. Our main experiments focus on policy transfer from Boston to Singapore, as this pair involves two different continents with differences in driving side (investigated in Appendix J), road geometry, and traffic rules. We report the results for other city pairs in Section 7.5, however, unless stated otherwise, the results refer to a Boston-to-Singapore transfer by default. For the zero-shot baseline π^0 , we train a trajectory planning model using behavior cloning (BC) using cross-entropy loss with trajectories from the source city. The network architecture and training hyperparameters are detailed in Appendix A and B, respectively. We also train its counterpart in the target city for comparison. Additional baselines include random and constant velocity policies, along with an oracle from logged demonstrations. We also report several diagnostic variants, including a variant with additional supervision beyond NOMAD. During adaptation, we initialize the network backbone and the actor head of π_θ with π^0 but learn the critic head from scratch. We set the interaction budget as 1 billion (approximately three days on a single NVIDIA A100) in all experiments to ensure a plateau of both the realism meta score and success rate. During evaluation, all dynamic vehicles are controlled by our policy; results involving other sim agents are reported separately in Appendix I.

7. Results

7.1. Main Results

Figure 3 (a) visualizes the empirical Pareto frontier of success rate versus realism meta score across different training checkpoints throughout self-play training in Boston-to-Singapore transfer (training curves are provided in Figure 17). Each point represents an adapted policy (checkpoint) $\pi^+ \in \Pi^+(C)$ with the color shade indicating the number of interaction steps since the beginning of training. The yellow star denotes π_0 , while the lime star shows behavior cloning using Singapore data. The modest performance of behavior cloning with 3,200 Singapore scenarios reflects the inherent data demands of imitation learning: empirical scaling analyzes in autonomous driving show that imitation-based policies are quite data hungry, with robustness and generalization improving only with substantially larger and more diverse datasets, while compounding errors dominate at smaller scales (Baniodeh et al., 2025) (Further discussion and realism submetrics for BC are provided in Figure 10). By contrast, NOMAD achieves better success–realism trade-offs even without demonstrations in the target city, indicating that map-based self-play can be a more effective adaptation strategy than imitation on limited data even when some target-city trajectories are available.

Interestingly, the resulting Pareto frontier forms a clear upper envelope and dominates both the zero-shot transfer policy π^0 and behavior cloning trained on 3,200 Singapore scenarios. This dominance spans the entire spectrum of success–realism trade-offs, which means that regardless of the desired balance between these two objectives, NOMAD offers a policy that outperforms both baselines in both metrics simultaneously. This means that practitioners may select a deployment policy π^{deploy} anywhere along this frontier, from conservative settings that prioritize realism to aggressive settings that maximize task completion, while still benefiting from substantial improvements over zero-shot transfer. Surprisingly, the observed trade-off between success rate and realism is mild: substantial gains in success rate are achieved with only marginal reductions in realism (a 7-percentage-point gain in success rate corresponds to only a 0.012 decrease in realism). Therefore, in practice, one can simply select the checkpoint with the highest success rate, without requiring target-city trajectories to estimate realism meta scores. Results of sub-metrics can be found in Figure 10. In addition, we do hold-out evaluation in Appendix K to assess potential selection bias, i.e., overestimation when constructing the empirical Pareto frontier.

To ground the frontier visualization with concrete values, Table 1 reports the success rate and realism meta score of representative baselines, the oracle policy, and the range spanned by the NOMAD Pareto frontier. NOMAD consistently achieves superior success–realism trade-offs com-

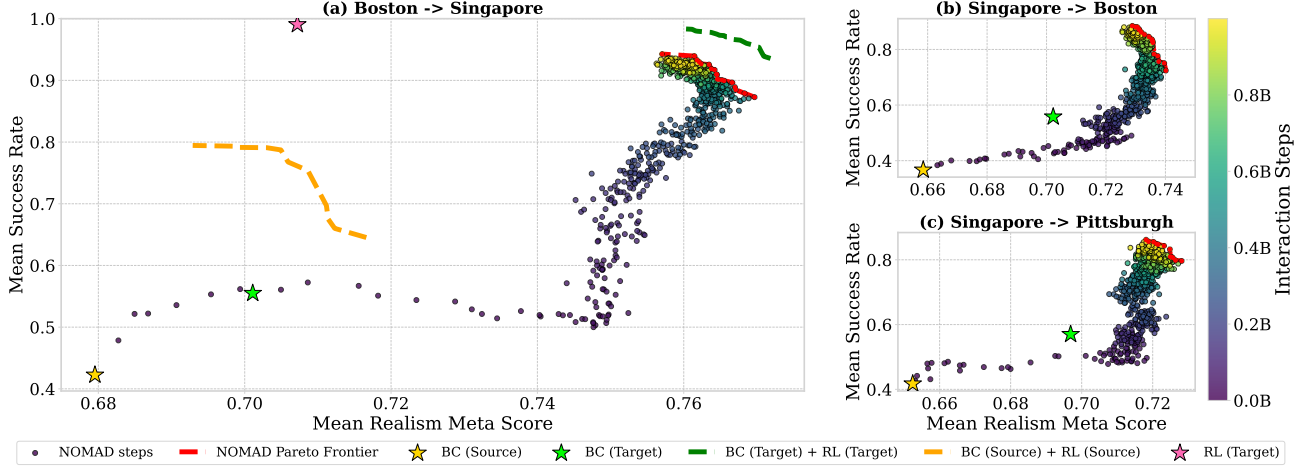


Figure 3. Success-realism trade-offs under city transfer. We plot mean success rate versus mean realism meta score over 5 runs for three transfer settings: (a) Boston-to-Singapore (primary), (b) Singapore-to-Boston, and (c) Singapore-to-Pittsburgh. Each dot is a NOMAD training checkpoint, colored by the cumulative number of interaction steps; the red dashed curve denotes the empirical Pareto frontier over NOMAD checkpoints. Stars and dashed curves denote reference policies and ablations: the zero-shot transfer behavior cloning policy from the source city π^0 (BC (Source)), behavior cloning with target-city demonstrations (BC (Target)), BC pretrained, self-play with logged target-city scenarios (BC (Target) + RL (Target)), BC pretrained, self-play with logged source-city scenarios (BC (Source) + RL (Source)), and RL from scratch in the target city with generated scenarios (RL (Target)).

pared to zero-shot transfer and other baselines, approaching the expert-derived upper bound without access to any target-city demonstrations.

Table 1. Success rate and realism meta score for representative baselines and NOMAD in closed-loop evaluation for Singapore. π_d^{expert} denotes an oracle policy obtained by inferring actions from logged expert trajectories and discretizing them to match the action space; its realism meta score serves as an approximate upper bound under the current POSG formulation.

Policy	Realism Meta Score	Success Rate
π_d^{expert}	0.8056	88.26%
Random	0.4074	4.30%
Constant Velocity	0.6147	19.45%
π^0	0.6795	42.25%
BC (Singapore)	0.7011	55.49%
NOMAD Frontier	0.7570~0.7697	87.28~94.27%

7.2. The Role of Behavioral Priors

NOMAD demonstrates that map-based self-play can effectively adapt a driving policy to a new city using only a simple reward function, which raises a natural question: *is an imitation policy necessary to initialize and regularize policy learning?* To answer this, we conduct an ablation study in which we train the policy purely via map-based self-play in the target city without regularization from scratch, using the same reward function and training budget. “RL (Target)” in Figure 3 shows the performance of the best checkpoint (training curves are provided in Figure 18). Without an imitation policy, self-play can indeed achieve near-

perfect success rates and improved realism meta score, compared to zero-shot transfer and behavior cloning policies in the target city. However, its realism meta score converges to a relative lower value. By contrast, NOMAD improves the success rate while maintaining a high realism meta score, ultimately achieving a substantially better success-realism trade-off.

To understand the source of this gap, we compare the kinematic metrics between these two methods in Figure 4 (other metrics are compared in Figure 14). Self-play without pre-training and regularization fails to learn high kinematic scores. While NOMAD exhibits a mild decline in kinematic realism due to the absence of explicit realism rewards, its initialization from behavioral priors provides a superior starting point compared to training from scratch. Also, by anchoring the self-play process to this human-like prior, NOMAD maintains significantly higher kinematic scores throughout the adaptation horizon. These results highlight that self-play alone is insufficient for learning realistic driving behavior under minimal reward supervision. The pretrained BC policy both serves as an optimization warm-start and provides critical behavioral priors that constrain exploration to human driving patterns and mitigates reward hacking. This enables NOMAD to achieve superior realism without sacrificing task success.

7.3. The Necessity of Target-City Map

To investigate the role of the target-city map in the adaptation process, we conduct behavior cloning followed by self-play with logged scenarios entirely in the *source* city

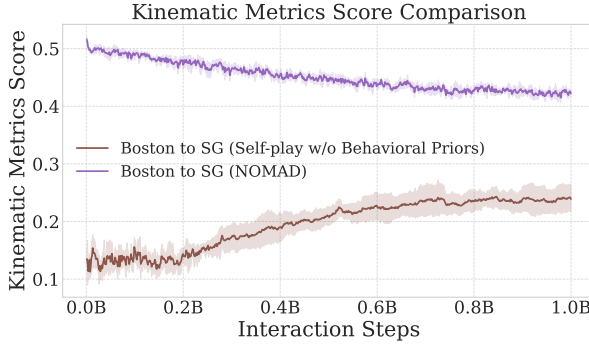


Figure 4. Comparison of kinematic metrics between self-play with and without behavioral priors. Self-play without behavioral priors struggles to learn kinematically realistic behavior, while NOMAD preserves substantially more realistic motion patterns despite lacking explicit kinematic rewards.

(Boston) and evaluate the resulting policy zero-shot in the target city (Singapore). This baseline uses the same BC initialization and self-play training protocol as NOMAD, but never accesses the target-city map or scenarios during training.

The “BC (Source) + RL (Source)” in Figure 3 shows the Pareto frontier of source-city self-play (detailed results are provided in Figure 15). While this baseline improves upon the zero-shot transfer policy, its Pareto frontier remains significantly inferior to that of NOMAD. Specifically, self-play conducted in Boston saturates at substantially lower success rates and yields marginal gains in realism when evaluated in Singapore.

These findings provide strong justification for map-based self-play in the *target* city. Self-play alone is not a silver bullet: improvements learned through interaction are largely city-specific and do not reliably transfer across distinct urban environments. Effective adaptation requires interaction dynamics to be grounded in the geometry, topology, and traffic structure of the deployment city, rather than relying solely on additional optimization in the source city.

7.4. NOMAD vs. Demonstration-Based Training

We further examine how closely NOMAD can approach the performance of a policy trained with access to target-city demonstrations. Specifically, we compare NOMAD, which uses neither target-city demonstrations nor logged scenarios, against a data-driven policy trained with access to 3,200 scenarios with human driving trajectories from Singapore. This policy is first pretrained via BC and subsequently trained using self-play on both generated and logged scenarios. The reward function, training budget, and overall training protocol are identical to those of NOMAD, with the only difference being that all training is

conducted directly using target-city demonstrations.

This policy, denoted as “BC (Target) + RL (Target)” in Figure 3 (full results in Figure 16), achieves only a modest improvement over NOMAD along the success–realism Pareto frontier. Notably, the performance gap between this policy and NOMAD is substantially smaller than the gap between NOMAD and zero-shot transfer. This indicates that map-based self-play provides the majority of the gains typically provided by target-city demonstrations.

7.5. Generalization to Other Cities

To verify that the effectiveness of NOMAD is not specific to a single target city, we evaluate cross-city transfer from Singapore to both Boston and Pittsburgh. Figure 3 (b) and (c) report the success–realism Pareto frontiers for these two transfer settings, respectively. These results demonstrate that NOMAD consistently delivers significant performance gains across different target cities. In all cases, the adapted policies substantially outperform the zero-shot baseline, despite the absence of any demonstrations from Boston or Pittsburgh. In particular, this generalization is achieved using a single reward function and a shared set of hyperparameters (Table 7) across all target cities, highlighting the robustness and scalability of NOMAD. It is worth noting that realism score value is city-dependent (Table 8), and the value between different cities is not comparable. Some qualitative results are provided in Appendix L.

7.6. Sensitivity Study on KL Regularization Strength

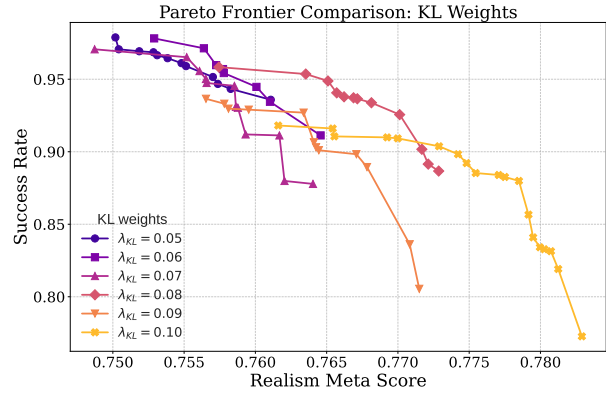


Figure 5. Pareto frontiers of success rate versus realism meta score for different KL weights. Smaller KL weights favor higher success at the cost of realism, while larger KL weights encourage more realistic behaviors but constrain success rate.

We evaluate how KL divergence coefficient λ_{KL} in Equation 8 influences the balance between success rate and behavioral realism during city transfer. Figure 5 presents Pareto frontiers for different values of λ_{KL} in Boston-to-Singapore transfer. Higher KL coefficients constrain the

policy to remain closer to the source-city prior, resulting in higher realism meta score but limiting the policy’s ability to adapt to target-city geometries, manifested as lower success rates. The results reveal that the values of λ_{KL} at around 0.08 achieve the best balance. Importantly, even with relatively aggressive or conservative KL regularization choices, NOMAD can still substantially outperform the zero-shot baseline. In our experiments, we use the $\lambda_{KL} = 0.08$ for all city pairs.

8. Conclusion and Future Work

This paper challenges a central assumption in city transfer in autonomous driving: that effective adaptation to a new city requires collecting human demonstrations in that city. We introduce NOMAD, a framework that adapts autonomous driving policies to new cities using only target-city map and its meta-information, without requiring any human demonstrations from them. Through extensive closed-loop evaluations, we show that NOMAD consistently expands the success-realism Pareto frontier, transforming brittle zero-shot transfer into a diverse set of policies that trade-off task success and behavioral realism. These results suggest that much of the disparity in optimal driving behavior across cities is determined at the map-level, which can be effectively addressed through map-based self-play.

Challenges remain. For example, differences in driving culture and social conventions across cities and countries continue to pose obstacles, highlighting the need for richer representations of interaction norms beyond geometric map structure. As traffic simulation continues to improve, we believe that scalable multi-agent self-play offers a viable and principled path toward robust, large-scale deployment of autonomous driving.

9. Acknowledgments

Compute for this project is graciously provided by the Isambard-AI National AI Research Resource, under the project “Robustness via Self-Play RL.” Some experiments were also made possible by a generous equipment grant from NVIDIA. Zilin Wang is funded by a generous grant from Waymo. Daphne Cornelisse is partially supported by the Cooperative AI Foundation and a Chishiki-AI SCiPE Fellowship. Bidipta Sarkar is supported by the Clarendon Fund Scholarship in partnership with a Department of Engineering Science Studentship for his Oxford DPhil. Alex David Goldie is funded by the EPSRC Centre for Doctoral Training in Autonomous Intelligent Machines and Systems EP/S024050/1. Jakob Nicolaus Foerster is partially funded by the UKRI grant EP/Y028481/1 (originally selected for funding by the ERC). The authors thank Lukas

Seier, Theo Wolf, Zengyuan Guo, Nathan Monette, Yulin Wang, Shashank Reddy, Juan Duque, Tingchen Fu and Darius Muglich for helpful discussions.

Impact Statement

This paper presents work whose goal is to accelerate expansion of autonomous driving systems. There are many potential societal consequences of such systems, none of which we feel merit being specifically highlighted here.

References

- Baniodeh, M., Goel, K., Ettinger, S., Fuertes, C., Seff, A., Shen, T., Gulino, C., Yang, C., Jerfel, G., Choe, D., et al. Scaling laws of motion forecasting and planning—a technical report. *arXiv preprint arXiv:2506.08228*, 2025.
- Bard, N., Foerster, J. N., Chandar, S., Burch, N., Lanctot, M., Song, H. F., Parisotto, E., Dumoulin, V., Moitra, S., Hughes, E., et al. The hanabi challenge: A new frontier for ai research. *Artificial Intelligence*, 280:103216, 2020.
- Caesar, H., Kabzan, J., Tan, K. S., Fong, W. K., Wolff, E., Lang, A., Fletcher, L., Beijbom, O., and Omari, S. nuplan: A closed-loop ml-based planning benchmark for autonomous vehicles. *arXiv preprint arXiv:2106.11810*, 2021.
- Cao, W., Hallgarten, M., Li, T., Dauner, D., Gu, X., Wang, C., Miron, Y., Aiello, M., Li, H., Gilitschenski, I., Ivanovic, B., Pavone, M., Geiger, A., and Chitta, K. Pseudo-simulation for autonomous driving. In *Conference on Robot Learning (CoRL)*, 2025.
- Chang, W.-J., Rangesh, A., Joseph, K., Strong, M., Tomizuka, M., Hu, Y., and Zhan, W. Spacer: Self-play anchoring with centralized reference models. *arXiv preprint arXiv:2510.18060*, 2025.
- Cornelisse, D. and Vinitsky, E. Human-compatible driving partners through data-regularized self-play reinforcement learning. *arXiv preprint arXiv:2403.19648*, 2024.
- Cornelisse*, D., Cheng*, S., Mandavilli, P., Hunt, J., Joseph, K., Doulazmi, W., Charraut, V., Gupta, A., Suarez, J., and Vinitsky, E. PufferDrive: A fast and friendly driving simulator for training and evaluating RL agents, 2025. URL <https://github.com/Emerge-Lab/PufferDrive>.
- Cornelisse, D., Pandya, A., Joseph, K., Suárez, J., and Vinitsky, E. Building reliable sim driving agents by scaling self-play. *arXiv preprint arXiv:2502.14706*, 2025.
- Cui, J., Tang, C., Holtz, J., Nguyen, J., Allievi, A. G., Qiu, H., and Stone, P. Talking vehicles: Cooperative driving via natural language. 2025.

- Cusumano-Towner, M., Hafner, D., Hertzberg, A., Huval, B., Petrenko, A., Vinitsky, E., Wijmans, E., Killian, T., Bowers, S., Sener, O., et al. Robust autonomy emerges from self-play. *arXiv preprint arXiv:2502.03349*, 2025.
- De Witt, C. S., Gupta, T., Makoviichuk, D., Makoviychuk, V., Torr, P. H., Sun, M., and Whiteson, S. Is independent learning all you need in the starcraft multi-agent challenge? *arXiv preprint arXiv:2011.09533*, 2020.
- Di Lillo, L., Gode, T., Zhou, X., Atzei, M., Chen, R., and Victor, T. Comparative safety performance of autonomous-and human drivers: A real-world case study of the waymo driver. *Heliyon*, 10(14), 2024.
- Dosovitskiy, A., Ros, G., Codevilla, F., Lopez, A., and Koltun, V. CARLA: An open urban driving simulator. In *Proceedings of the 1st Annual Conference on Robot Learning*, pp. 1–16, 2017.
- Feng, L., Bahari, M., Amor, K. M. B., Zablocki, É., Cord, M., and Alahi, A. Unitraj: A unified framework for scalable vehicle trajectory prediction. In *European Conference on Computer Vision*, pp. 106–123. Springer, 2024.
- Fu, H., Zhang, D., Zhao, Z., Cui, J., Liang, D., Zhang, C., Zhang, D., Xie, H., Wang, B., and Bai, X. Orion: A holistic end-to-end autonomous driving framework by vision-language instructed action generation. *arXiv preprint arXiv:2503.19755*, 2025.
- Gulino, C., Fu, J., Luo, W., Tucker, G., Bronstein, E., Lu, Y., Harb, J., Pan, X., Wang, Y., Chen, X., et al. Waymax: An accelerated, data-driven simulator for large-scale autonomous driving research. *Advances in Neural Information Processing Systems*, 36:7730–7742, 2023.
- Hansen, E. A., Bernstein, D. S., and Zilberstein, S. Dynamic programming for partially observable stochastic games. In *AAAI*, volume 4, pp. 709–715, 2004.
- Hu, A., Russell, L., Yeo, H., Murez, Z., Fedoseev, G., Kendall, A., Shotton, J., and Corrado, G. Gaia-1: A generative world model for autonomous driving. *arXiv preprint arXiv:2309.17080*, 2023.
- Hu, H., Lerer, A., Peysakhovich, A., and Foerster, J. “other-play” for zero-shot coordination. In *International Conference on Machine Learning*, pp. 4399–4410. PMLR, 2020.
- Jeon, M., Seo, J., and Min, J. Da-raw: Domain adaptive object detection for real-world adverse weather conditions. In *2024 IEEE International Conference on Robotics and Automation (ICRA)*, pp. 2013–2020. IEEE, 2024.
- Kazemkhani, S., Pandya, A., Cornelisse, D., Shacklett, B., and Vinitsky, E. GPUDrive: Data-driven, multi-agent driving simulation at 1 million FPS. In *The Thirteenth International Conference on Learning Representations*, 2025. URL <https://openreview.net/forum?id=ERv8ptegFi>.
- Kesting, A., Treiber, M., and Helbing, D. Enhanced intelligent driver model to access the impact of driving strategies on traffic capacity. *Philosophical Transactions of the Royal Society A*, 368(1928):4585–4605, 2010. doi: 10.1098/rsta.2010.0084.
- Knox, W. B., Allievi, A., Banzhaf, H., Schmitt, F., and Stone, P. Reward (mis) design for autonomous driving. *Artificial Intelligence*, 316:103829, 2023.
- Kusano, K. D., Scanlon, J. M., Chen, Y.-H., McMurry, T. L., Gode, T., and Victor, T. Comparison of waymo rider-only crash rates by crash type to human benchmarks at 56.7 million miles. *Traffic Injury Prevention*, pp. 1–13, 2025.
- Leussink, D. and Freed, J. Waymo to begin data collection in tokyo with driver-operated test rides, April 2025. URL <https://www.reuters.com/business/autos-transportation/waymo-begin-data-collection-tokyo-with-driver-ope>. Published April 10, 2025; updated April 10, 2025. Reporting by Daniel Leussink; editing by Jamie Freed.
- Li, B., Wang, Y., Mao, J., Ivanovic, B., Veer, S., Leung, K., and Pavone, M. Driving everywhere with large language model policy adaptation. In *Proceedings of the IEEE/CVF Conference on Computer Vision and Pattern Recognition*, pp. 14948–14957, 2024a.
- Li, L., Lyu, J., Ma, G., Wang, Z., Yang, Z., Li, X., and Li, Z. Normalization enhances generalization in visual reinforcement learning. In *AAMAS*, 2024b.
- Li, Q., Peng, Z., Feng, L., Zhang, Q., Xue, Z., and Zhou, B. Metadrive: Composing diverse driving scenarios for generalizable reinforcement learning. *IEEE transactions on pattern analysis and machine intelligence*, 45(3):3461–3475, 2022.
- Michaelis, C., Mitzkus, B., Geirhos, R., Rusak, E., Bringmann, O., Ecker, A. S., Bethge, M., and Brendel, W. Benchmarking robustness in object detection: Autonomous driving when winter is coming. *arXiv preprint arXiv:1907.07484*, 2019.
- Montali, N., Lambert, J., Mougin, P., Kuefler, A., Rhinehart, N., Li, M., Gulino, C., Emrich, T., Yang, Z., Whiteson, S., et al. The waymo open sim agents challenge. *Advances in Neural Information Processing Systems*, 36: 59151–59171, 2023.

- Muhammad, K., Hussain, T., Ullah, H., Del Ser, J., Rezaei, M., Kumar, N., Hijji, M., Bellavista, P., and De Albuquerque, V. H. C. Vision-based semantic segmentation in scene understanding for autonomous driving: Recent achievements, challenges, and outlooks. *IEEE Transactions on Intelligent Transportation Systems*, 23(12):22694–22715, 2022.
- Pan, A., Bhatia, K., and Steinhardt, J. The effects of reward misspecification: Mapping and mitigating misaligned models. In *International Conference on Learning Representations*, 2022. URL <https://openreview.net/forum?id=JYtwGwIL7ye>.
- Peng, Z., Li, Q., Hui, K. M., Liu, C., and Zhou, B. Learning to simulate self-driven particles system with coordinated policy optimization. *Advances in neural information processing systems*, 34:10784–10797, 2021.
- Philion, J., Peng, X. B., and Fidler, S. Trajeglish: Traffic modeling as next-token prediction. In *The Twelfth International Conference on Learning Representations*, 2024. URL <https://openreview.net/forum?id=Z59Rb5bPPP>.
- Ren, X., Lu, Y., Cao, T., Gao, R., Huang, S., Sabour, A., Shen, T., Pfaff, T., Wu, J. Z., Chen, R., et al. Cosmos-drive-dreams: Scalable synthetic driving data generation with world foundation models. *arXiv preprint arXiv:2506.09042*, 2025.
- Renz, K., Chen, L., Arani, E., and Sinavski, O. Simplingo: Vision-only closed-loop autonomous driving with language-action alignment. In *Proceedings of the Computer Vision and Pattern Recognition Conference*, pp. 11993–12003, 2025.
- Russell, L., Hu, A., Bertoni, L., Fedoseev, G., Shotton, J., Arani, E., and Corrado, G. Gaia-2: A controllable multi-view generative world model for autonomous driving. *arXiv preprint arXiv:2503.20523*, 2025.
- Sakaridis, C., Dai, D., Hecker, S., and Van Gool, L. Model adaptation with synthetic and real data for semantic dense foggy scene understanding. In *Proceedings of the european conference on computer vision (ECCV)*, pp. 687–704, 2018.
- Shao, H., Hu, Y., Wang, L., Song, G., Waslander, S. L., Liu, Y., and Li, H. Lmdrive: Closed-loop end-to-end driving with large language models. In *Proceedings of the IEEE/CVF Conference on Computer Vision and Pattern Recognition*, pp. 15120–15130, 2024.
- Sima, C., Renz, K., Chitta, K., Chen, L., Zhang, H., Xie, C., Beißwenger, J., Luo, P., Geiger, A., and Li, H. Drivelm: Driving with graph visual question answering. In *European conference on computer vision*, pp. 256–274. Springer, 2024.
- Sun, X., Jiang, Y., Burnett, G., Bai, J., and Bai, R. A cross-cultural analysis of driving styles for future autonomous vehicles. *Advanced Design Research*, 1(2):71–77, 2023.
- Tian, X., Gu, J., Li, B., Liu, Y., Wang, Y., Zhao, Z., Zhan, K., Jia, P., Lang, X., and Zhao, H. DriveVLM: The convergence of autonomous driving and large vision-language models. In *8th Annual Conference on Robot Learning*, 2024. URL <https://openreview.net/forum?id=928V4Umlys>.
- Treibler, M. and Kesting, A. *Traffic Flow Dynamics: Data, Models and Simulation*. Springer, Berlin, Heidelberg, 2013. doi: 10.1007/978-3-642-32460-4.
- Treibler, M., Hennecke, A., and Helbing, D. Congested traffic states in empirical observations and microscopic simulations. *Physical Review E*, 62(2):1805–1824, 2000. doi: 10.1103/PhysRevE.62.1805.
- Vasudevan, A. B., Peri, N., Schneider, J., and Ramanan, D. Planning with adaptive world models for autonomous driving. In *2025 IEEE International Conference on Robotics and Automation (ICRA)*, pp. 14938–14945. IEEE, 2025.
- Vinitsky, E., Lichtlé, N., Yang, X., Amos, B., and Foerster, J. Nocturne: a scalable driving benchmark for bringing multi-agent learning one step closer to the real world. *Advances in Neural Information Processing Systems*, 35:3962–3974, 2022.
- Wang, J., Sun, H., Yan, X., Feng, S., Gao, J., and Liu, H. X. Terasim-world: Worldwide safety-critical data synthesis for end-to-end autonomous driving. *arXiv preprint arXiv:2509.13164*, 2025.
- Wang, X., Zhu, Z., Huang, G., Chen, X., Zhu, J., and Lu, J. Drivedreamer: Towards real-world-drive world models for autonomous driving. In *European conference on computer vision*, pp. 55–72. Springer, 2024.
- Waymo. Bringing waymo to more people, sooner, August 2025a. URL <https://waymo.com/blog/2025/08/bringing-waymo-to-more-people-sooner>. Accessed: 2025-12-22.
- Waymo. Where waymo is driving, December 2025b. URL <https://waymo.com/rides/#rides-map>. Accessed: 2025-12-22.
- Wayve. The ai-500 roadshow: 500 cities and what we learned, 2025. URL <https://wayve.ai/thinking/ai-500-roadshow-500-cities/>. Accessed: 2025-01-07.

Wu, W., Feng, X., Gao, Z., and Kan, Y. Smart: Scalable multi-agent real-time motion generation via next-token prediction. *Advances in Neural Information Processing Systems*, 37:114048–114071, 2024.

Wurman, P. R., Barrett, S., Kawamoto, K., MacGlashan, J., Subramanian, K., Walsh, T. J., Capobianco, R., Devlic, A., Eckert, F., Fuchs, F., et al. Outracing champion gran turismo drivers with deep reinforcement learning. *Nature*, 602(7896):223–228, 2022.

Yasarla, R., Han, S., Cheng, H.-P., Liu, L., Mahajan, S., Bhattacharyya, A., Shi, Y., Garrepalli, R., Cai, H., and Porikli, F. Roca: Robust cross-domain end-to-end autonomous driving. *arXiv preprint arXiv:2506.10145*, 2025.

Yu, C., Velu, A., Vinitsky, E., Gao, J., Wang, Y., Bayen, A., and Wu, Y. The surprising effectiveness of ppo in cooperative multi-agent games. *Advances in neural information processing systems*, 35:24611–24624, 2022.

Zhang, C., Vinyals, O., Munos, R., and Bengio, S. A study on overfitting in deep reinforcement learning. *arXiv preprint arXiv:1804.06893*, 2018.

Zhang, C., Biswas, S., Wong, K., Fallah, K., Zhang, L., Chen, D., Casas, S., and Urtasun, R. Learning to drive via asymmetric self-play. In *European Conference on Computer Vision*, pp. 149–168. Springer, 2024.

Zhang, Z., Karkus, P., Igl, M., Ding, W., Chen, Y., Ivanovic, B., and Pavone, M. Closed-loop supervised fine-tuning of tokenized traffic models. In *Proceedings of the Computer Vision and Pattern Recognition Conference*, pp. 5422–5432, 2025.

Contents

A Network Architecture and Observation Visualization	14
A.1 Policy Network Architecture	14
A.2 Visualization of Observation	14
B Detailed Experimental Setup	15
C Scenario Generation	17
C.1 Scenario Generation Algorithm	17
C.2 Parameter Specification	18
D Examples of Scenarios	19
D.1 Logged Scenarios	19
D.2 Generated Scenarios	19
E Metric Definitions	21
E.1 WOSAC Realism Evaluation Metric	21
E.2 Additional Metrics	22
F Sub-Metric Analysis	24
G Influence of Behavior Priors on Sub-Metrics	29
H Extended Experimental Results	30
H.1 The Necessity of Target-City Map	30
H.2 NOMAD vs. Demonstration-Based Training	30
H.3 NOMAD Training Curves	30
H.4 The Role of Behavioral Priors	31
I Evaluation Under Non-Self-Play Test-Time Agents	33
I.1 Log-Replay: Removing Co-Adaptation at Test Time	33
I.2 Cross-Play: Convention Consistency Across Independently Trained Agents	35
J Effect of Map Mirroring for Opposite-Side Driving	43
K Additional Hold-Out Evaluation of Selected Frontier Checkpoints	44
L Qualitative results	47

A. Network Architecture and Observation Visualization

A.1. Policy Network Architecture

We adopt a shared actor-critic architecture with a modular observation encoder, as shown in Figure 6. At each timestep, the policy receives three structured inputs: ego-centric state features, observations of surrounding agents (illustrated in Figure 7), and road-level information derived from the map. Each modality is first processed by a dedicated embedding layer, and the resulting embeddings are fused by a shared observation encoder composed of stacked fully connected layers with residual connections. The encoded representation is then passed to two separate branches. The actor branch outputs incremental trajectory commands $(\delta_x, \delta_y, \delta_h)$, representing relative position and heading updates, while the critic branch predicts a scalar value estimate v_θ . Both branches employ residual blocks with normalization and dropout to stabilize training and improve generalization across cities.

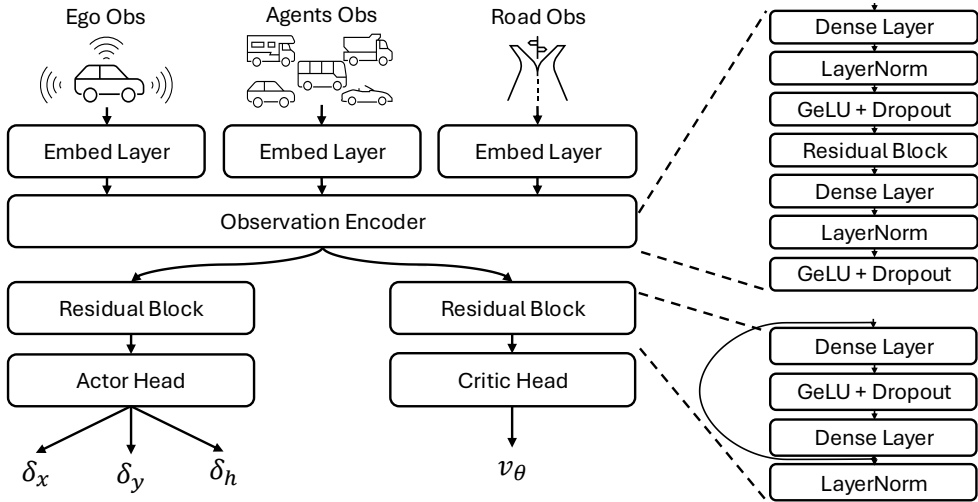


Figure 6. Policy Network architecture. The policy consists of modality-specific embedding layers for ego state, surrounding agents, and road observations, followed by a shared observation encoder. The encoded features are passed to separate actor and critic branches with residual blocks. The actor outputs trajectory increments $(\delta_x, \delta_y, \delta_h)$, while the critic predicts the scalar state value v_θ .

A.2. Visualization of Observation

We provide an example of observation of our agents in Figure 7.

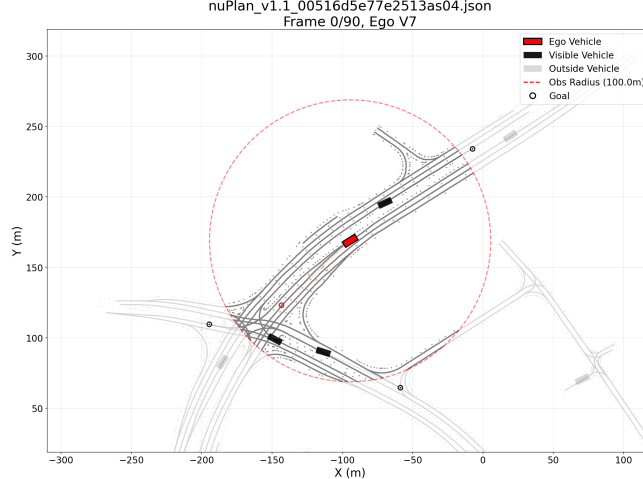


Figure 7. Visualization of the ego-centric observation space.

B. Detailed Experimental Setup

The hyperparameters of the network used in the experiments are shown in Table 2.

Table 2. Network hyperparameters.

Hyperparameter	Value
Observation Dim	2984
Observation Embedding Dim	64×3
Encoder Width	512
Dropout	0.01
Residual Block Num	1
Projection Width	256
Pre-head Width	256

The detailed setting of our environment is shown in Table 3. We deployed a discretized action space. This design is motivated by these considerations: First, continuous actions introduce additional optimization challenges under hard constraints, e.g., prediction–execution mismatch caused by clipping or squashing in continuous RL algorithms. In addition, discretization offers multi-modal exploration and stable policy gradient estimation. And for imitation learning, a common practice in autonomous driving, it mitigates averaging in continuous regression and improves imitation of multi-modal expert behavior. Furthermore, empirically, compared to inverse bicycle models, delta-pose actions enable better replay of expert trajectories, leading to a higher success rate of policy with inferred expert actions. However, since this abstraction bypasses vehicle dynamics and actuation constraints, it may induce lower kinematic realism.

Table 3. Environment configurations.

Hyperparameter	Value
Observation Radius	50.0
Max Controllable Agents Num	64
Max Road Observation Num	200
Ego observation	1×6
Agents Observation	$(64-1) \times 6$
Road Observation	200×13
Action Space Type	Multi-Discrete
δ_x	$[-2.0, 2.0, 256]$
δ_y	$[-2.0, 2.0, 256]$
δ_h	$[-3.14/4, 3.14/4, 256]$
Action Space Size	256^3
Goal Reaching Reward	1.0
Collision Reward	-0.75
Offroad Reward	-0.75
Goal Reaching Behavior	Disappear
Collision Behavior	Ignore
Offroad Behavior	Ignore
Goal Distance Threshold	2.0
Initial Step	0
Horizon	90

Hyperparameters of behavior cloning and PPO are shown in Table 4 and Table 5, respectively.

Table 4. Behavior Cloning hyperparameters.

Hyperparameters	Value
Dataset Scenario Num	3200
Batch Size	64
Loss Function	Cross Entropy
Learning Rate	1e-3
Weight Decay	1e-2
Scheduler	Cosine Annealing

Table 5. PPO hyperparameters.

Hyperparameters	Value
World Num	1,000
Batch Size	8,192
Buffer Size	131,072
Update Epoch	4
Discount Factor γ	0.99
GAE Discount Factor λ	0.95
Advantage Normalization	True
Clip Coefficient ϵ	0.2
Value Loss Weight	0.3
Entropy Loss Weight	1e-4
KL Weight	0.08
Max Gradient Norm	0.5
Total Timestep	1 billion

C. Scenario Generation

C.1. Scenario Generation Algorithm

Given a lane-level map segment m from the target city, our heuristic scenario generation method $\Xi_\varphi(\cdot|m, I_C)$ produces a traffic scenario $\xi = (s_0, \{g^i\}_{i=0}^{N-1}, m)$. Unlike logged scenarios that contain full trajectories, a generated scenario only specifies the initial conditions: the initial state $s_0 = \{(p^i, \psi^i, v^i)\}_{i=0}^{N-1}$, where each vehicle i is characterized by its initial position $p^i \in \mathbb{R}^2$, heading ψ^i , and speed v^i , along with its goal position $g^i \in \mathbb{R}^2$. The trajectory connecting s_0 to the goals is produced by the learned policy during simulation. The generation process consists of four phases.

First, we extract lane centerlines (polylines) \mathcal{L} from the map and construct a directed lane connectivity graph G that encodes valid lane-to-lane successors. **Second**, we determine the number of vehicles by sampling a traffic density ρ (vehicles per kilometer) from a city-specific Gamma distribution, $\rho \sim \text{Gamma}(\alpha, \theta) + \rho_0$, where α is the shape parameter, θ is the scale parameter, and ρ_0 is a location shift. This distribution can be obtained via urban traffic sensors or aerial imagery. We compute the number of dynamic vehicles as $N_{\text{dyn}} = \max(1, \lfloor \rho \cdot \sum_{\ell \in \mathcal{L}} \text{len}(\ell) / 1000 \rfloor)$, and optionally add static (parked) vehicles with probability p_{static} . **Third**, we place vehicles on the lane network using rejection sampling with collision avoidance. For each candidate, we sample a lane segment (ℓ, s) with probability proportional to segment length, compute the centerline position and heading, and apply small Gaussian perturbations for lateral offset and heading noise. Dynamic vehicle speeds are sampled from a LogNormal distribution calibrated to traffic flow statistics (see below). We enforce a minimum safe distance $d_{\text{safe}} = \max(v \cdot \Delta t_{\text{gap}}, d_{\text{min}})$, where Δt_{gap} is the minimum time gap and d_{min} is the minimum spatial separation. **Fourth**, we generate goals by traversing the lane graph G . For static vehicles, $g^i = p^i$. For dynamic vehicles, we sample a target travel distance $d_{\text{goal}} \sim \mathcal{N}(\kappa_\mu v^i, \kappa_\sigma v^i)$, where κ_μ and κ_σ are coefficients that scale the mean and standard deviation of the goal distance proportionally to the vehicle's initial speed v^i . The sampled distance

Algorithm 1 Heuristic Scenario Generation $\Xi_\varphi(\cdot|m, I_C)$

Input: Map segment m , city meta-information I_C , parameters φ

Output: Traffic scenario $\xi = (s_0, \{g^i\}_{i=0}^{N-1}, m)$

```

// Phase 1: Build lane network
1:  $\mathcal{L}, G \leftarrow \text{EXTRACTLANENETWORK}(m)$ 
// Phase 2: Determine vehicle count from  $I_C$ 
2:  $\rho \sim \text{Gamma}(\alpha, \theta) + \rho_0$  {City-specific density}
3:  $N_{\text{dyn}} \leftarrow \max(1, \lfloor \rho \cdot \text{TotalLaneLength}(\mathcal{L}) / 1000 \rfloor)$ 
4:  $N_{\text{static}} \leftarrow \text{SAMPLESTATICCOUNT}(N_{\text{dyn}}, p_{\text{static}})$ 
// Phase 3: Place vehicles with collision avoidance
5:  $\mathcal{V} \leftarrow \emptyset$ 
6: for  $i = 0$  to  $N_{\text{dyn}} + N_{\text{static}} - 1$  do
7:    $\text{is\_static} \leftarrow (i \geq N_{\text{dyn}})$ 
8:    $(p, \psi) \leftarrow \text{SAMPLELANEPOSITION}(\mathcal{L})$  {With Gaussian perturbations}
9:    $v \leftarrow 0$  if  $\text{is\_static}$  else  $\text{SAMPLESPEED}()$ 
10:  if  $\text{COLLISIONFREE}(p, v, \mathcal{V}, \Delta t_{\text{gap}}, d_{\text{min}})$  then
11:     $\mathcal{V} \leftarrow \mathcal{V} \cup \{(p, \psi, v, \text{is\_static})\}$ 
12:  end if
13: end for
14:  $N \leftarrow |\mathcal{V}|$  {Final vehicle count}
// Phase 4: Generate goals via lane graph traversal
15: for each  $(p^i, \psi^i, v^i, \text{static}^i) \in \mathcal{V}$  do
16:   if  $\text{static}^i$  then
17:      $g^i \leftarrow p^i$ 
18:   else
19:      $d_{\text{goal}} \leftarrow \text{SAMPLEGOALDISTANCE}(v^i, \kappa_\mu, \kappa_\sigma)$ 
20:      $g^i \leftarrow \text{ADVANCEONGRAPH}(G, \mathcal{L}, p^i, d_{\text{goal}})$ 
21:   end if
22: end for
23: return  $\xi = (s_0, \{g^i\}_{i=0}^{N-1}, m)$ 

```

is clipped to $[d_{\min}^g, d_{\max}^g]$, then we advance along successor lanes until the distance is exhausted or a dead-end is reached. Small Gaussian noise is added to the final goal position for robustness.

C.2. Parameter Specification

For reproducibility, we report all parameters φ used in the scenario generation algorithm. The city-specific traffic density parameters (Table 6) were estimated by fitting a Gamma distribution to vehicle density statistics computed from the nuPlan dataset for each target city using maximum likelihood estimation. While this uses aggregate density distributions from logged data, it does not use individual trajectory information. These statistics could alternatively be obtained from traffic sensors or aerial imagery.

Table 6. City-specific traffic density parameters for $\rho \sim \text{Gamma}(\alpha, \theta) + \rho_0$ (vehicles/km), where α is the shape and θ is the scale parameter.

City	α	ρ_0	θ
Boston	1.4694	0.1897	0.4252
Pittsburgh	2.1327	0.0000	0.3982
Singapore	1.2630	0.1363	0.2500

The shared parameters for vehicle placement and goal generation are reported in Table 7. Dynamic vehicle speeds are sampled from a LogNormal distribution with mean $\bar{v} = 0.85 \cdot v_{\max}$ and standard deviation $\sigma_v = 0.22 \cdot v_{\max}$, where v_{\max} is the maximum observed speed in the scenario. This reflects typical free-flowing traffic behavior where vehicles operate below maximum speed (Treiber & Kesting, 2013). The collision avoidance parameters—minimum time gap Δt_{gap} and minimum distance d_{\min} —are consistent with calibrated values from the Intelligent Driver Model (Treiber et al., 2000). For goal generation, the distance coefficients κ_μ and κ_σ determine how far ahead vehicles plan to travel based on their current speed: a vehicle traveling at speed v receives a goal at distance $d_{\text{goal}} \sim \mathcal{N}(\kappa_\mu v, \kappa_\sigma v)$, encouraging faster vehicles to have farther goals. Small Gaussian perturbations are added to lateral position, heading, and goal location for realism.

Table 7. Shared scenario generation parameters.

Category	Parameter	Value
<i>Vehicle Placement</i>	Minimum time gap Δt_{gap}	1.2 s
	Minimum distance d_{\min}	5.0 m
	Static vehicle probability p_{static}	0.5
<i>Speed Distribution</i>	Mean speed fraction \bar{v}/v_{\max}	0.85
	Speed std fraction σ_v/v_{\max}	0.22
<i>Goal Generation</i>	Distance mean coefficient κ_μ	9.0
	Distance std coefficient κ_σ	3.0
	Goal distance range $[d_{\min}^g, d_{\max}^g]$	[5, 200] m

D. Examples of Scenarios

D.1. Logged Scenarios

We visualize logged scenarios from different cities in Figure 8.

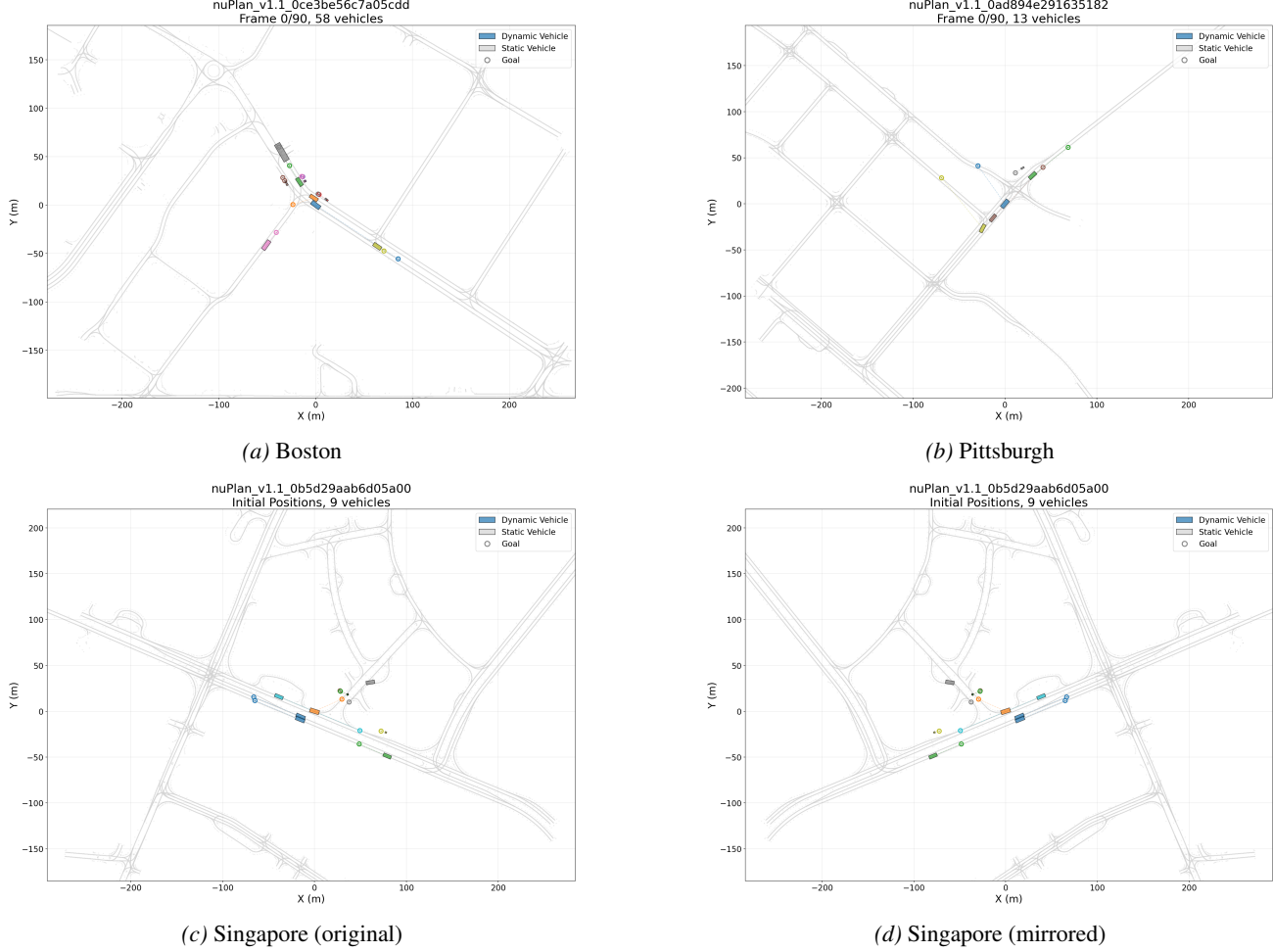


Figure 8. Visualization of scenarios from different cities in the nuPlan dataset. The rectangles denote vehicles and the circles with the corresponding color denote their goals. To mirror the Singapore and make it a right-hand traffic city, we first flip the scenario across x-axis, then we change the orientation of road edges while keeping the orientation of road lanes.

D.2. Generated Scenarios

Figure 9 demonstrates examples of generated scenarios on two sampled map segments from Singapore. Vehicles are demonstrated by colored rectangles, and their assigned goal points are illustrated using a circle with the same color. As it can be seen, vehicles are generated on drivable areas on all scenarios, and their corresponding goals are also generated on drivable areas at a reachable distance. Moreover, there are no overlapping vehicles on the map or vehicles with unrealistic headways. The illustration of two scenarios from the same map segment aims to demonstrate the effect of random generation of scenarios.

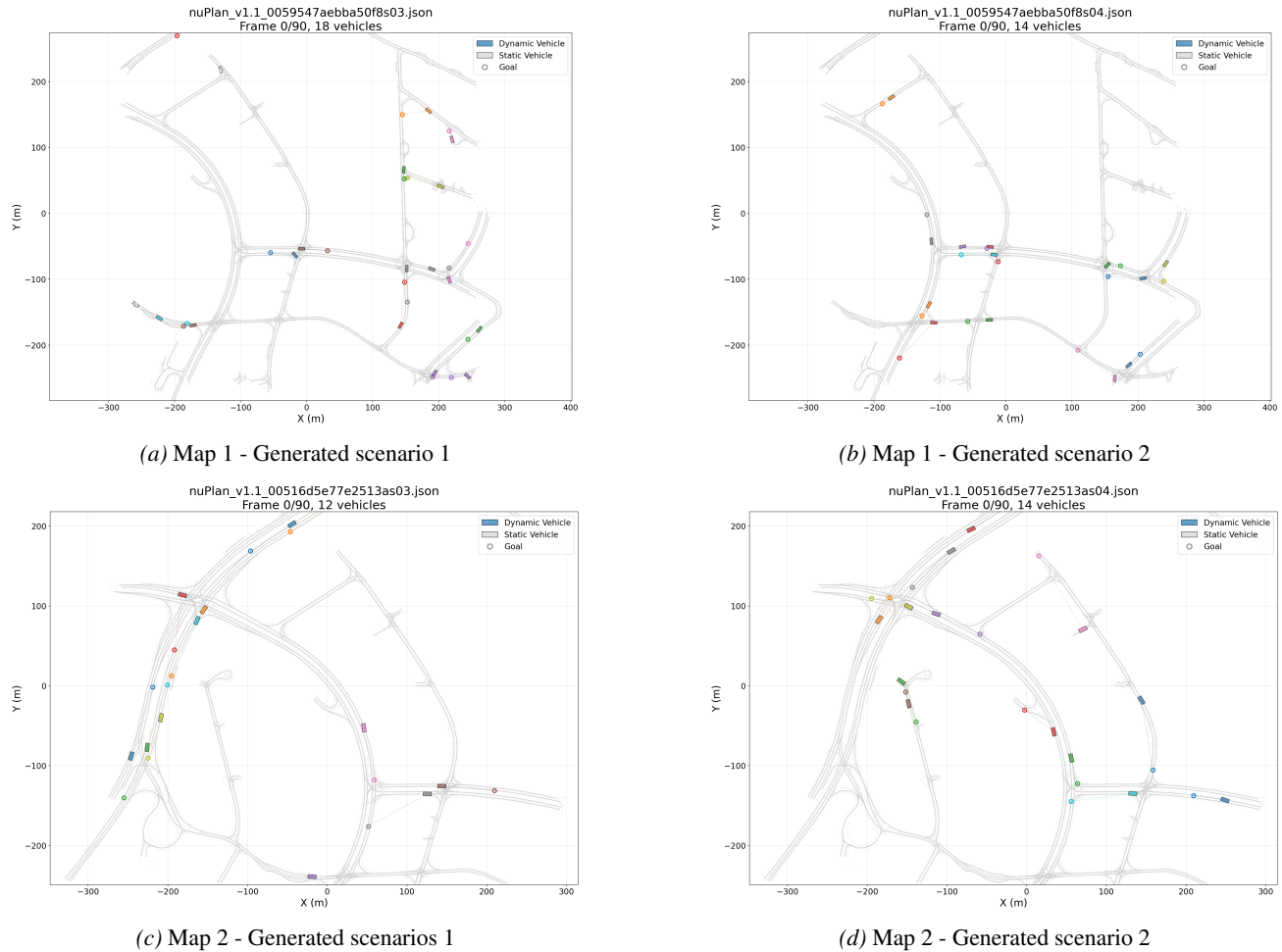


Figure 9. Examples of generated scenarios on Singapore map for two different sampled map segments.

E. Metric Definitions

E.1. WOSAC Realism Evaluation Metric

The Waymo Open Sim Agents Challenge (WOSAC) (Montali et al., 2023) is a benchmark for evaluating the realism of simulation agents in autonomous driving. The core idea behind WOSAC evaluation is that realistic simulation agents should produce behavior distributions that match the actual distribution of real-world driving scenarios observed in logged data. To quantify this, WOSAC computes the approximate negative log-likelihood (NLL) of logged human trajectories under the distribution induced by the simulation agent. Lower NLL (equivalently, higher likelihood) indicates that the simulated behaviors better match the distribution of real human driving. For evaluation, WOSAC requires agents to generate K rollouts per scenario.

E.1.1. COMPONENT METRICS.

WOSAC decomposes realism into nine interpretable component metrics organized into three categories rather than computing a single holistic likelihood over full trajectories. These three elements largely overlap with comfort/kinematics, TTC/collisions, and drivable-area compliance categories in nuPlan planning challenge. We favor WOSAC over nuPlan’s evaluation metrics because nuPlan’s metrics are predominantly threshold- and constraint-based validation and safety checks, whereas WOSAC provides a distributional measure of *humanlikeness* that aligns with our notion of realism.

The three components of the WOSAC metrics are detailed as follows:

Kinematic Metrics capture the motion dynamics of individual agents, measuring whether simulated vehicles move with human-like speed and acceleration profiles. Let $p_t = [p_t^x, p_t^y, p_t^z]^\top$ denote the position at timestep t , and θ_t denote the heading angle:

1. Linear Speed: $\|v_t\| = \|(p_{t+1} - p_t)/\Delta t\|_2$. This measures the instantaneous speed of the vehicle.
2. Linear Acceleration: $(\|v_{t+1}\| - \|v_t\|)/\Delta t$. This captures how aggressively the vehicle speeds up or slows down. Jerky or unnaturally aggressive acceleration patterns indicate unrealistic behavior.
3. Angular Speed: $\omega_t = d(\theta_{t+1}, \theta_t)/\Delta t$, where $d(\cdot, \cdot)$ computes the minimal angular difference on the unit circle. This measures how quickly the vehicle is turning.
4. Angular Acceleration: $d(\omega_{t+1}, \omega_t)/\Delta t$. This captures the smoothness of steering behavior.

Interaction Metrics capture multi-agent dynamics, measuring whether simulated vehicles interact with other road users in human-like ways:

5. Distance to Nearest Object: The signed distance to the nearest other object, computed via the GJK (Gilbert-Johnson-Keerthi) algorithm on bounding box polygons. Positive values indicate separation, while negative values indicate overlap (collision). unrealistic agents may follow too closely or maintain unnaturally large gaps.
6. Collisions: A binary indicator $\mathbf{1}\{\text{signed distance} < 0\}$ for whether a collision has occurred. While the distance metric captures the full distribution of proximity to other objects, collisions are weighted more heavily in the final score because they represent safety-critical failures.
7. Time-to-Collision (TTC): The estimated time before a collision would occur, assuming both vehicles maintain their current velocities. TTC captures the temporal safety margin that human drivers maintain.

Map-based Metrics measure whether simulated vehicles respect road boundaries and lane structures:

8. Distance to Road Edge: The signed distance to the nearest road boundary. Positive values indicate the vehicle is within the drivable area, while negative values indicate the vehicle has departed the road.
9. Road Departures (Offroad): A binary indicator for whether the vehicle has left the drivable area. Like collisions, road departures are weighted more heavily.

E.1.2. TIME-SERIES NLL COMPUTATION

For each component metric j , WOSAC computes a score by comparing the distribution of feature values from the logged human trajectory against the empirical distribution from K simulated rollouts. The score is computed as an average over the time axis with validity masking to handle agents that may enter or exit the scene. Let $\mathcal{V}_t \in \{0, 1\}$ denote the validity indicator at timestep t (indicating whether the agent is active):

$$m_j = \exp \left(-\frac{1}{\sum_{t=0}^{H-1} \mathbb{1}(\mathcal{V}_t)} \sum_{t=0}^{H-1} \mathbb{1}(\mathcal{V}_t) \cdot \text{NLL}_{j,t} \right), \quad (9)$$

where H is the horizon length. The per-timestep $\text{NLL}_{j,t}$ is estimated by constructing a histogram-based categorical distribution over the K sampled feature values, with Laplace smoothing to avoid infinite NLL for out-of-distribution logged values. The exponential transformation maps the average NLL to the $[0, 1]$ range, where higher values indicate greater realism (i.e., the logged human behavior is more likely under the simulated distribution).

E.1.3. FINAL REALISM META SCORE – COMPOSITE METRIC

Let $|\mathcal{D}|$ denote the number of test scenarios and $M = 9$ the number of component metrics. The final realism meta score aggregates all component metrics via a weighted average:

$$\mathcal{M}^K = \frac{1}{|\mathcal{D}| \cdot M} \sum_{i=1}^{|\mathcal{D}|} \sum_{j=1}^M w_j \cdot m_{i,j}^K, \quad \text{where} \quad \sum_{j=1}^M w_j = 1, \quad (10)$$

where w_j denotes the weight for metric j . Following WOSAC, we set the weights for collision and road departure metrics to be twice as large as other components. This weighting emphasizes safety-critical behaviors, reflecting the fact that collisions and road departures are unambiguous indicators of unrealistic driving that human drivers almost never exhibit.

The WOSAC composite metric \mathcal{M}^K provides a tractable approximation to our realism meta score $R(\pi, C)$ defined in Equation 2: rather than estimating the full trajectory likelihood $\log q_\pi(\tau|\xi)$ directly, WOSAC decomposes it into interpretable feature-level NLLs computed by comparing logged human trajectories $\tau \sim p(\cdot|\xi)$ against K rollouts from the policy $q_\pi(\cdot|\xi)$. Throughout the paper, we use “realism meta score” and “WOSAC realism meta score” interchangeably.

E.1.4. REALISM SCORE IS CITY-DEPENDENT

In addition, we investigate whether the realism meta score between different cities is comparable by evaluating the realism of human trajectories in different cities. The results are reported in Table 8, where π_c^{expert} denotes continuous inferred actions from logged demonstrations, which provide an empirical upper bound on realism, and π_d^{expert} denotes discretized inferred actions used to train behavior cloning (BC) policies. The different realism meta scores achieved by π_c^{expert} across cities indicate that realism is inherently city-dependent and should therefore be interpreted comparatively within the same city rather than in absolute terms across different cities.

Table 8. Performance of expert policies in different cities.

Policy	Scenarios	Realism Meta Score	Success Rate
π_c^{expert}	Boston	0.8311	100.0%
	Singapore	0.8581	100.0%
π_d^{expert}	Boston	0.7814	85.47%
	Singapore	0.8056	88.26%

E.2. Additional Metrics

We report collision rate and offroad rate separately, while they are already captured within the WOSAC interaction and map-based component metrics, respectively. Beyond the WOSAC realism meta score, we report the Average Displacement Error (ADE) as a supplementary metric. We compute ADE as the mean L2 distance between the position of the simulated

agent and the position of the logged human trajectory at corresponding timesteps:

$$\text{ADE} = \frac{1}{|\mathcal{D}|} \sum_{i=1}^{|\mathcal{D}|} \frac{1}{H} \sum_{t=1}^H \|p_t^{\pi, (i)} - p_t^{\log, (i)}\|_2, \quad (11)$$

where $p_t^{\pi, (i)}$ denotes the position of the agent controlled by policy π at timestep t in scenario i , and $p_t^{\log, (i)}$ denotes the corresponding position from the logged human trajectory.

Unlike open-loop trajectory prediction tasks, where ADE measures prediction accuracy against a fixed ground truth, in closed-loop evaluation, ADE should be interpreted as a measure of behavioral similarity rather than prediction accuracy. This means that lower ADE indicates that the policy produces trajectories that remain closer to what a human driver executed in the same scenario, even though the two trajectories evolve under different closed-loop dynamics. We include ADE as a complementary reference metric, while recognizing that the WOSAC realism meta score provides a more principled distributional measure of human-likeness.

F. Sub-Metric Analysis

Following Section E, and taking the transfer from Boston to Singapore as an example, Figure 10 decomposes the realism meta score into its constituent components: kinematic metrics, interactive metrics, and map-based metrics. The kinematic score, which captures velocity and acceleration profiles, exhibits a declining trend as training progresses, decreasing from approximately 0.51 to 0.42. This suggests that self-play improvements in success rate and the overall realism meta score come with some degradation in kinematics-related metrics. In contrast, the interactive metrics, measuring behaviors such as time-to-collision and collision avoidance, remain relatively stable throughout training, indicating that the adapted policy preserves safe interaction patterns learned from the source city. Most notably, the map-based metrics show substantial improvement, rising from approximately 0.55 to above 0.87, which reflects the policy’s increasing ability to comply with Singapore’s distinct road geometries and lane structures. Finally, the average displacement error (ADE) improves substantially from approximately 9 to around 7. Lower ADE values indicate that the planned trajectory stays closer to the ground-truth trajectory on average over time. Note that ADE is not a good metric for closed-loop evaluation, since completely imitating expert trajectories is not our goal.

Overall, these results suggest that effective city adaptation via map-based self-play improves the realism scores in most of the realism sub-metrics. However, this decomposition also highlights a trade-off: while NOMAD improves the overall realism meta score and reduces ADE, it comes with a modest degradation in kinematics metrics. This suggests that matching the target-city trajectory structure is easier than fully recovering speed and acceleration profiles. These kinematics gaps could potentially be mitigated through more targeted reward design, which is beyond the scope of the study.

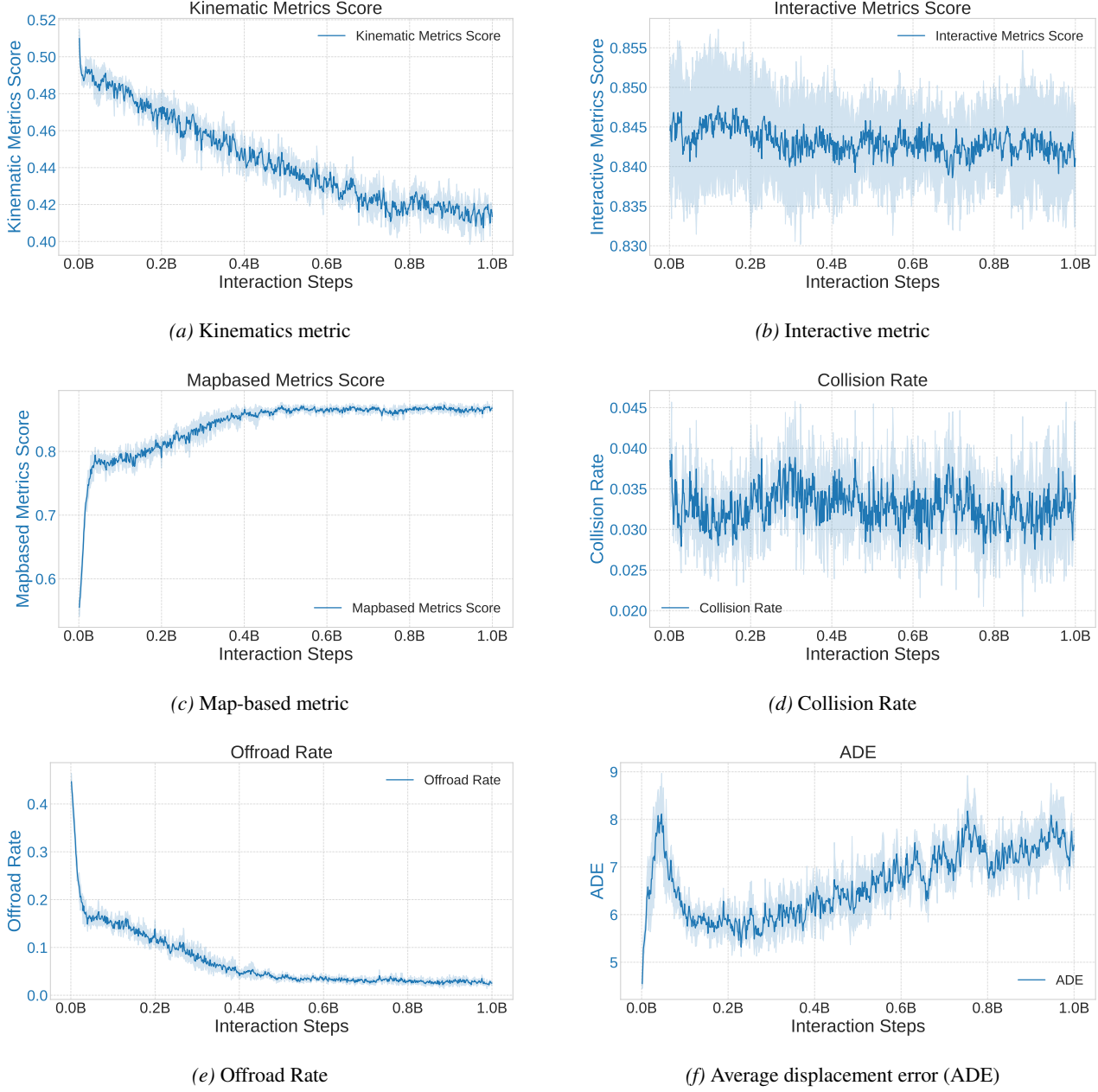


Figure 10. Detailed sub-metrics in realism metric and ADE in the experiment of transferring from Boston to Singapore. Although the BC policy (at the beginning of training) achieves reasonable kinematic smoothness, it frequently violates map constraints (e.g., off-road driving), leading to a poor map-based realism meta score. In our experiments, behavior cloning serves as a canonical source-city planner. While its absolute performance depends on dataset coverage, our focus is on the performance degradation induced by the lack of supervised finetuning in the target city and the ability of NOMAD to mitigate it without demonstrations.

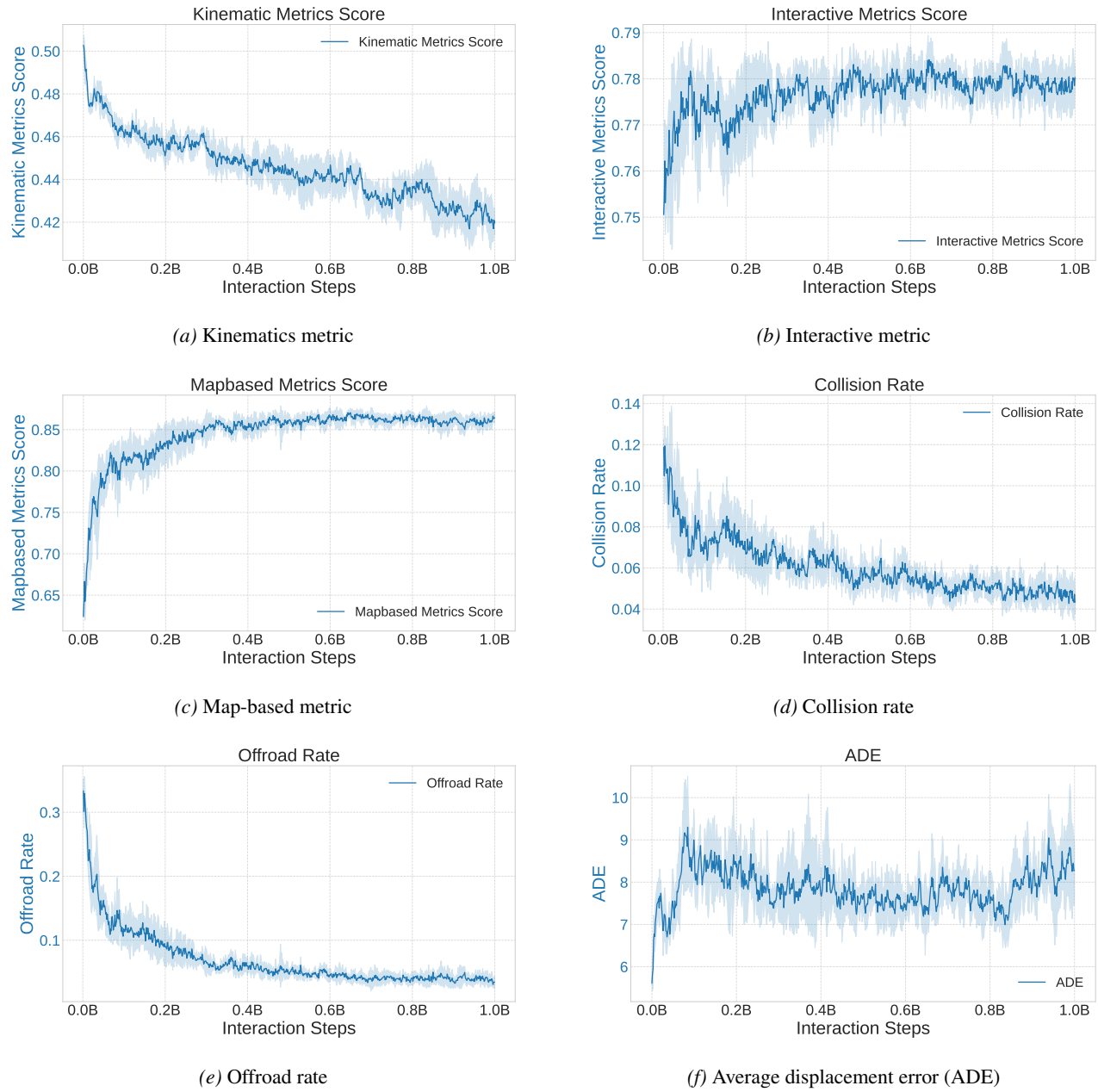


Figure 11. Detailed sub-metrics in realism metric and ADE in the experiment of transferring from Singapore to Boston.

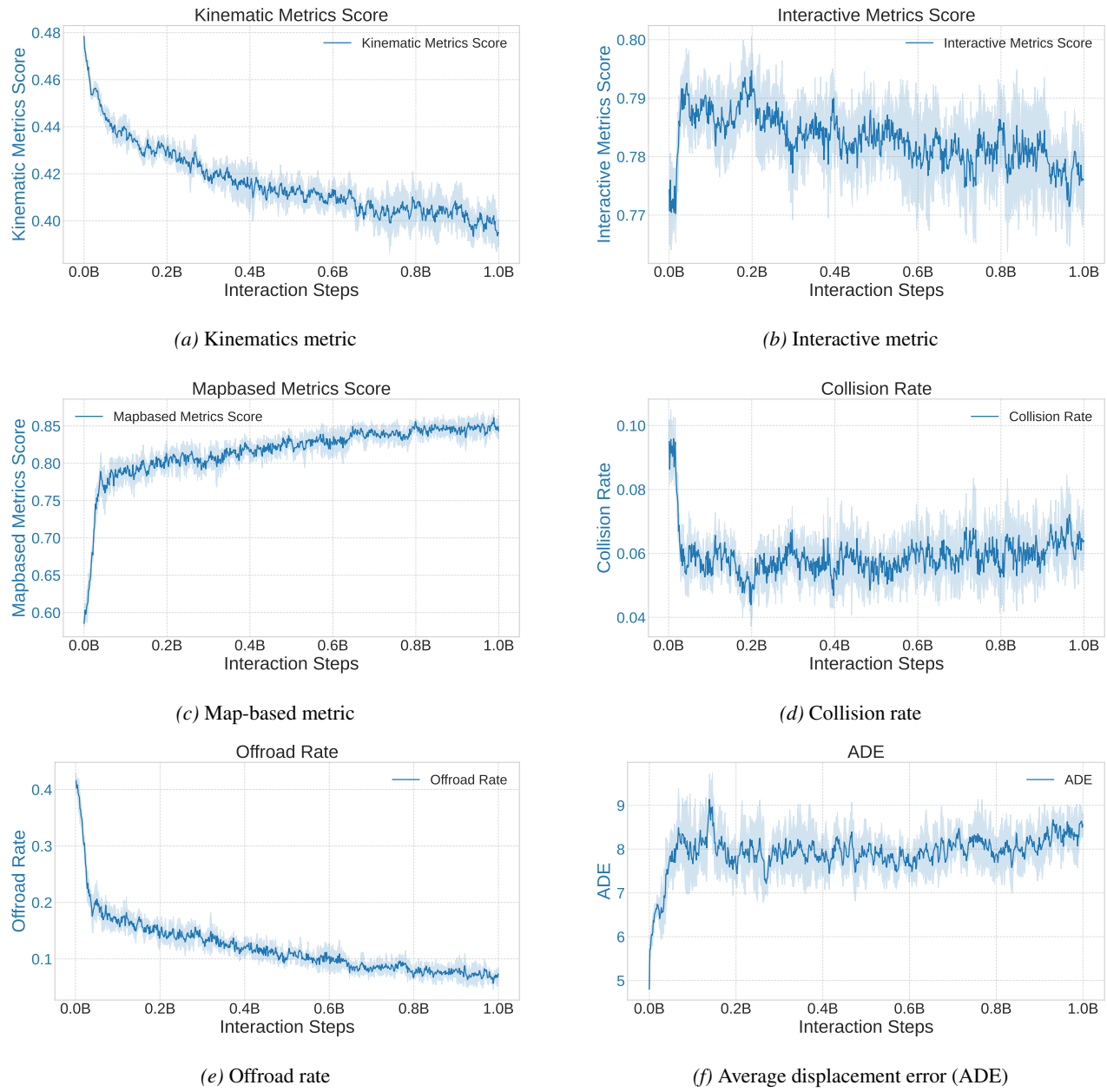


Figure 12. Detailed sub-metrics in realism metric and ADE in the experiment of transferring from Singapore to Pittsburgh.

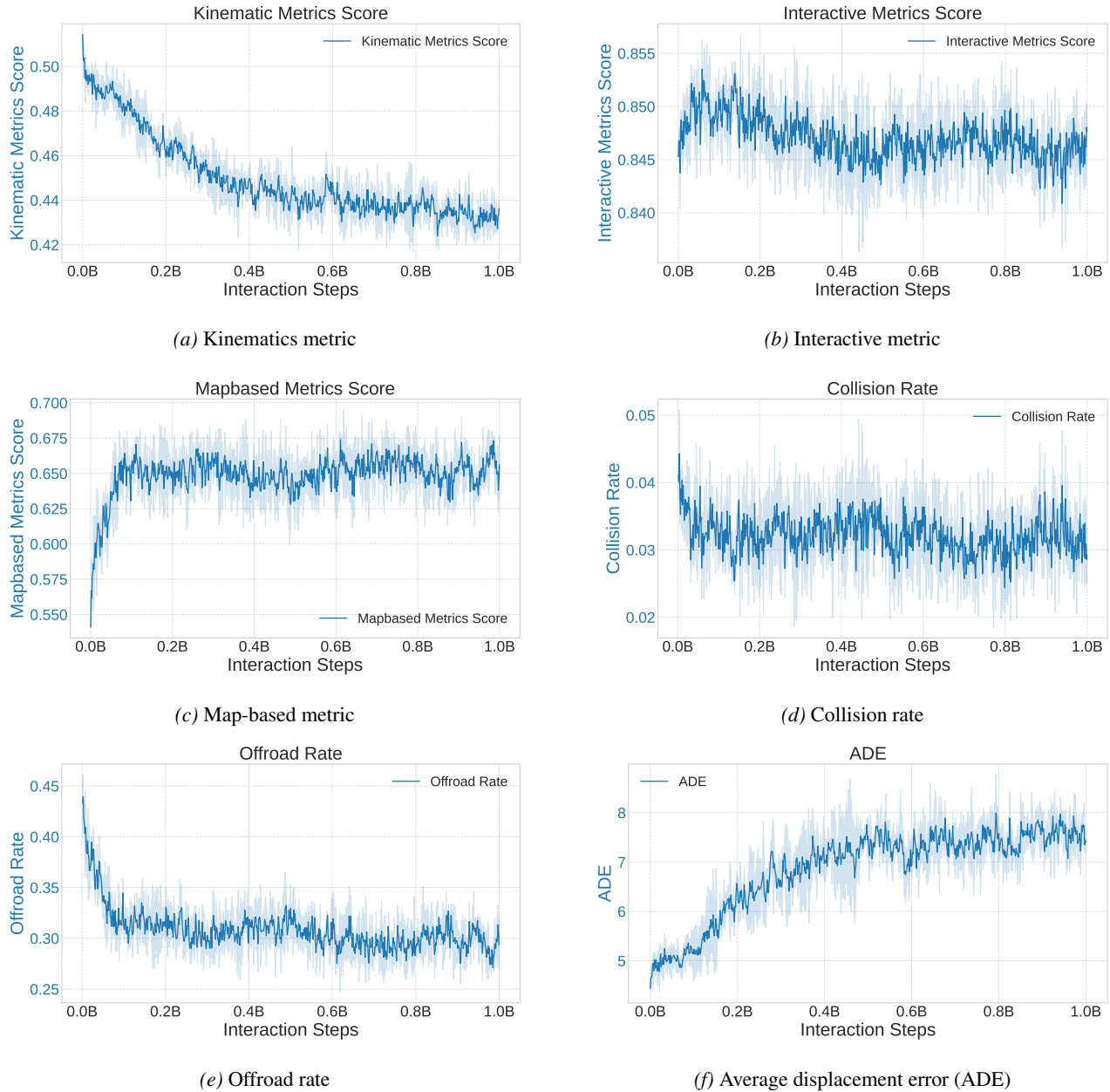


Figure 13. Detailed sub-metrics in realism metric and ADE in the experiment of doing both behavior cloning and self-play MARL in Boston, and then evaluation in Singapore.

G. Influence of Behavior Priors on Sub-Metrics

Figure 14 provides a detailed breakdown of training dynamics across individual evaluation metrics for map-based self-play with and without behavioral priors. While pure self-play (without BC initialization and regularization) is eventually able to improve interactive metrics and reduce collision rates, it consistently lags behind NOMAD in all the realism submetrics throughout training, as reflected by substantially lower kinematic and map-based scores. These results further substantiate that behavioral priors play a critical role in stabilizing self-play training and guiding exploration toward human-like driving behaviors under the supervision of a simple reward function.

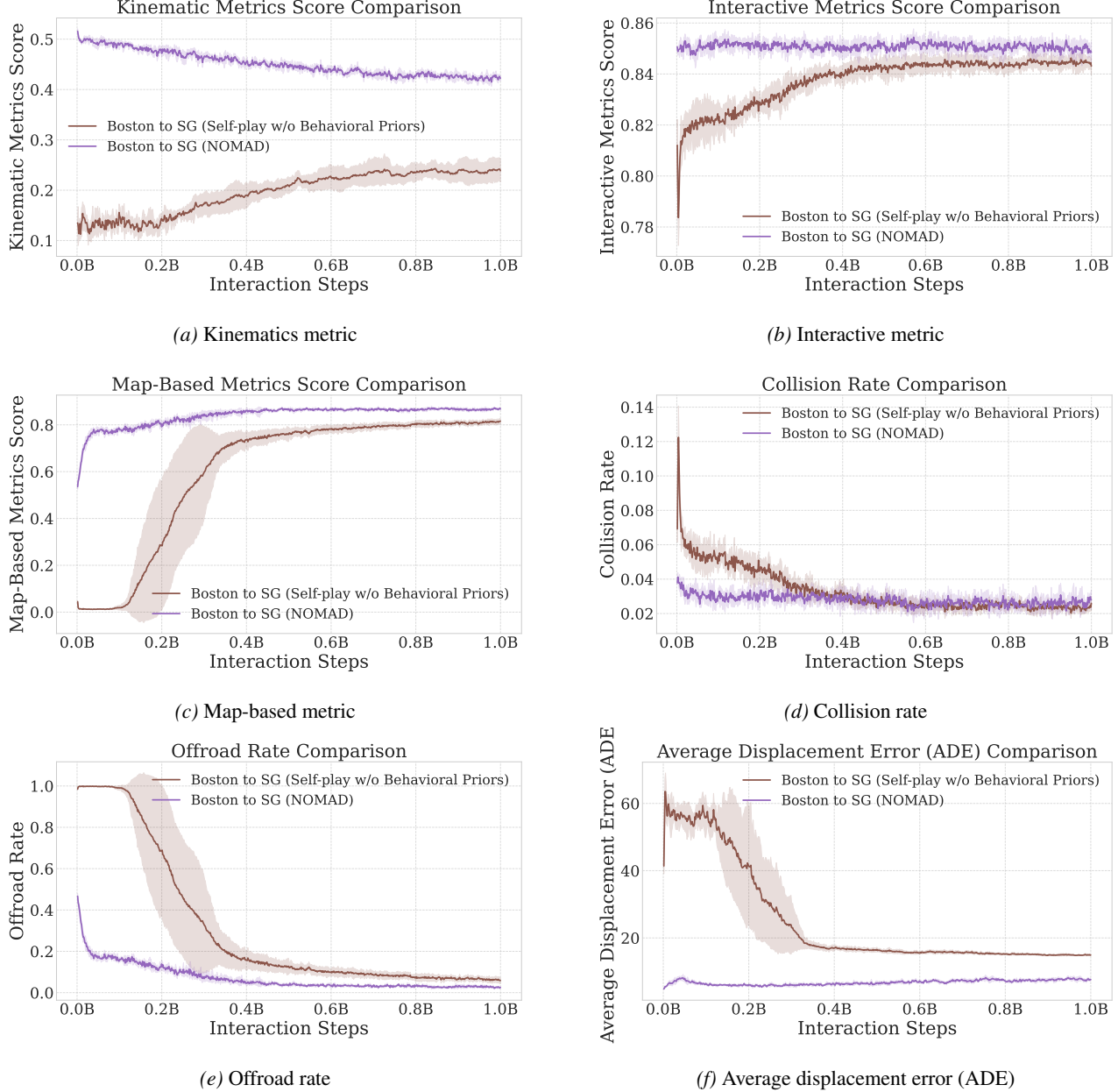


Figure 14. Comparison of all metrics between self-play with and without behavioral priors. Behavioral priors play a critical role in stabilizing self-play training and guiding exploration toward human-like driving under the supervision of a simple reward function.

H. Extended Experimental Results

H.1. The Necessity of Target-City Map

To assess the necessity of the target-city map and the agent interactions within it, we introduce an additional baseline, where we perform behavior cloning followed by self-play MARL using *logged scenarios* exclusively in the source city (Boston). Then, we evaluate the resulting policy zero-shot in the target city (Singapore). This baseline employs the same BC initialization and self-play training protocol as NOMAD but has no access to target-city maps or scenarios during training.

As shown in Figure 15, the red Pareto frontier (BC (Boston) + RL (Boston)) surpasses the zero-shot transfer policy but remains substantially below that of NOMAD (BC (Boston) + RL (Singapore)). Self-play (RL) in Boston saturates at considerably lower success rates and yields only marginal realism improvements when evaluated in Singapore. These results underscore the necessity of map-based self-play in the target city. In fact, effective adaptation requires grounding interaction dynamics in the geometry, topology, and traffic structure of the target city, rather than relying on pure optimization in the source city.

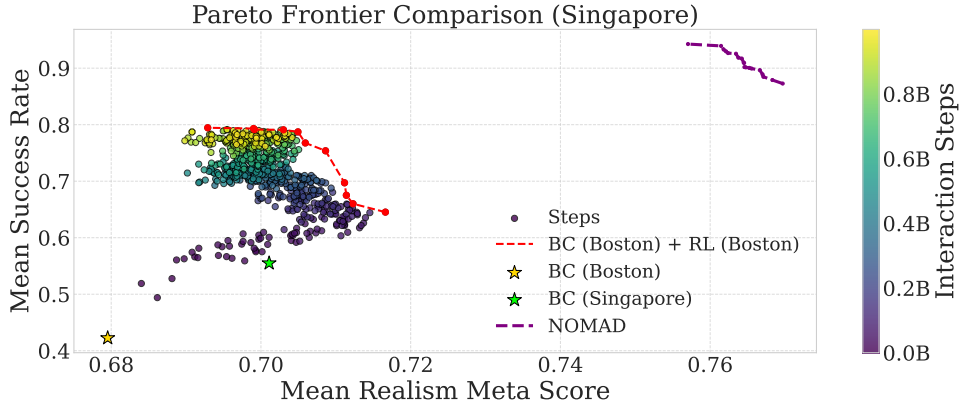


Figure 15. Source-city self-play is beaten by NOMAD. The dashed red curve (BC (Boston) + RL (Boston)) denotes policies trained with behavior cloning and self-play in Boston only, evaluated zero-shot in Singapore. The dashed purple curve denotes NOMAD. Source-city self-play improves over zero-shot transfer but fails to approach the Pareto frontier achieved by NOMAD, demonstrating that self-play must be grounded in the target-city map to effectively adapt across cities.

H.2. NOMAD vs. Demonstration-Based Training

We also investigate how closely NOMAD can match a policy trained with access to target-city demonstrations. Specifically, we compare NOMAD, which uses neither target-city demonstrations nor logged scenarios, against a data-driven policy trained on 3,200 scenarios with human driving trajectories from Singapore. This policy is pretrained via behavior cloning and subsequently trained using self-play MARL on *both generated and logged scenarios* in the target city. The reward function, training budget, and overall protocol are identical to NOMAD; the only difference is that all training occurs while accessing target-city demonstrations.

This policy, labeled “BC (Singapore) + RL (Singapore)” in Figure 16, achieves a modest improvement over NOMAD along the success–realism Pareto frontier. Notably, the performance gap between this policy and NOMAD is considerably smaller than the gap between NOMAD and zero-shot transfer. This suggests that map-based self-play captures most of the benefit typically achievable by target-city demonstrations, and that the primary source of cross-city performance degradation is effectively mitigated through interaction-aware self-play in the target-city simulator rather than direct supervision from target-city data.

H.3. NOMAD Training Curves

Figure 17 shows the training dynamics of NOMAD during adaptation from Boston to Singapore. Both the realism meta score and success rate are evaluated on the Singapore test set over the course of training. The success rate increases rapidly

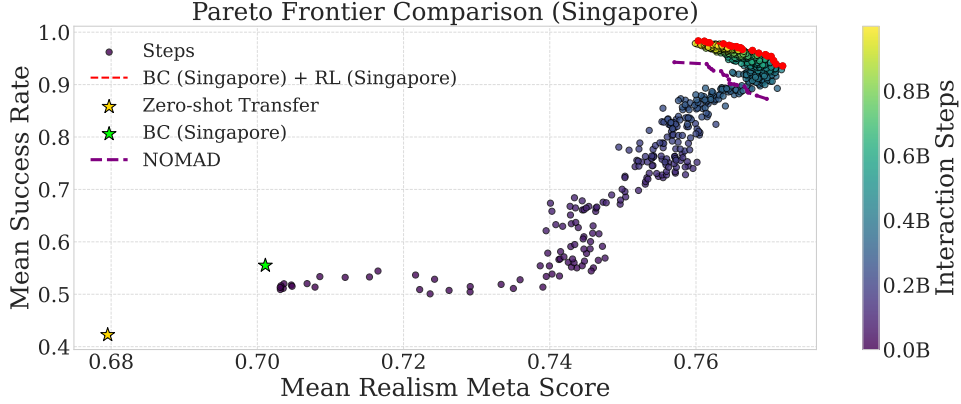


Figure 16. NOMAD closes most of the gap between zero-shot transfer and target-city demonstration-accessed policy. We compare zero-shot transfer, NOMAD (RL with generated scenarios), and a policy trained with 3,200 scenarios with logged trajectories in the target-city using the same BC+RL training protocol (BC (Singapore) + RL (Singapore)). While the policy with access to target-city demonstrations yields additional gains over NOMAD, this improvement is modest compared to the substantial gap between zero-shot transfer and NOMAD, highlighting the effectiveness of map-based self-play for city transfer.

in the early stages of training, rising from approximately 42% (the zero-shot baseline) to around 95% within the first 600 million interaction steps, and continues to improve gradually thereafter. The realism meta score exhibits a different trajectory: it increases sharply during the initial phase of training as the policy learns to comply with target-city map constraints, then plateaus and shows a mild decline in later stages as the policy prioritizes goal completion. This pattern reflects the success–realism trade-off discussed in the main text. Results are averaged over 5 independent runs, with shaded regions indicating 95% confidence intervals.

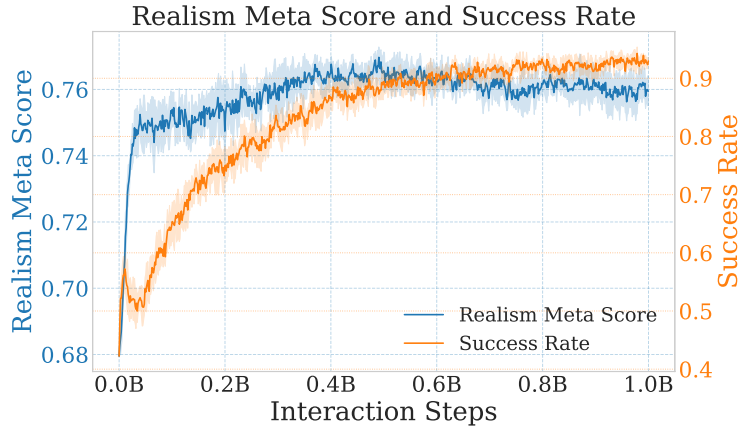


Figure 17. Realism meta score and success rate over interaction steps on the Singapore test scenarios. Results are shown with mean and 95% confidence interval over 5 seeds.

H.4. The Role of Behavioral Priors

Figure 18 shows the training dynamics of mere map-based self-play in Singapore without behavioral priors, corresponding to the ablation study in Section 7.2. In this setting, the policy is trained from scratch using only the reward signal, without behavior cloning initialization or KL regularization against a pretrained policy. The success rate starts near zero and increases steadily, eventually reaching near-perfect levels (99%) after approximately 600 million interaction steps. However, the realism meta score follows a notably different trajectory compared to NOMAD (Figure 17): it rises from a very low initial value as the policy learns basic driving behavior, but converges to a substantially lower plateau (around 0.65–0.70) compared to NOMAD’s final realism scores (around 0.76). This gap highlights the critical role of behavioral priors in

maintaining human-like driving patterns when optimizing with a minimal reward function. Results are averaged over 5 independent runs, with shaded regions indicating 95% confidence intervals.

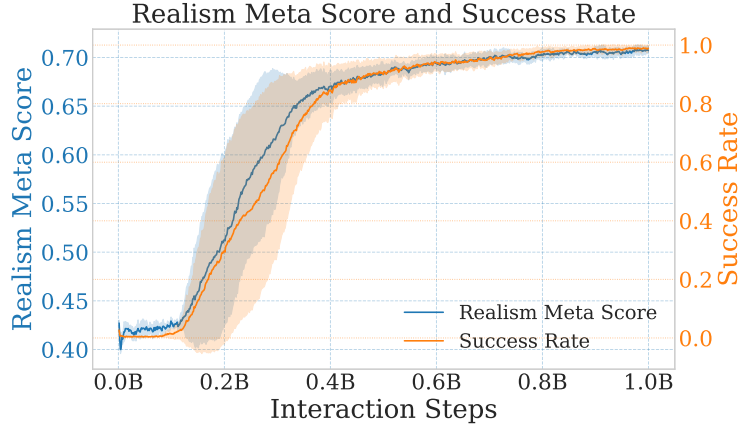


Figure 18. Realism meta score and success rate during map-based self-play without behavioral priors in Singapore. Self-play without pretraining and regularization achieves near-perfect success but a lower realism meta score. Shaded regions indicate 95% confidence interval across 5 runs.

I. Evaluation Under Non-Self-Play Test-Time Agents

Autonomous driving policies are ultimately deployed in traffic with potentially *unseen* agents, raising the concern that multi-agent self-play might overfit to partner behaviors encountered during training (e.g., forming seed-specific conventions) (Bard et al., 2020). To address this, we supplement our standard self-play evaluation with two protocol variants that explicitly break the self-play assumption. First, *log-replay* evaluates the learned ego policy against non-reactive background vehicles that follow logged human trajectories, removing partner responsiveness and directly testing robustness under distribution shift. Second, *cross-play* evaluates coordination between independently trained policies (different random seeds) at the same Pareto-frontier checkpoints, testing whether performance depends on shared conventions within a single training run. Together, these experiments provide evidence that **NOMAD’s gains persist beyond self-play evaluation and are not driven by brittle co-adaptation to a particular set of training partners.**

I.1. Log-Replay: Removing Co-Adaptation at Test Time

To probe whether NOMAD’s self-play improvements rely on co-adaptation among learned agents, we perform a log-replay evaluation in which only the ego vehicle is controlled by the learned policy, while all other vehicles follow their logged trajectories. Figures 19, 20, and 21 show the results on Boston-to-Singapore, Singapore-to-Boston, and Singapore-to-Pittsburgh, respectively. Relative to self-play evaluation (Figure 3), we observe that the success rate decreases while realism meta score increases.

We attribute the lower success rate compared to self-play evaluation to the factor of convention losing: during training, the ego vehicle interacts with responsive self-controlled agents, whereas at test time log-replay agents do not follow the same interaction conventions; behaviors that succeed under self-play coordination (e.g., merges/yields that assume reciprocity) may fail when partners do not respond. In contrast, the higher realism may be induced by human-like interaction context: when surrounding vehicles follow human trajectories, the ego’s best-response actions tend to imitate typical human reactions (e.g., more conservative gap acceptance, yielding, and speed profiles), which are rewarded by our realism metric.

Importantly, these result differences do not affect our main claim. Although log-replay evaluation yields slightly different absolute success/realism values, **NOMAD consistently improves over the zero-shot policy by a large margin across all city pairs, indicating robust benefits that persist even when the ego is evaluated against non-reactive logged traffic rather than self-play partners.**

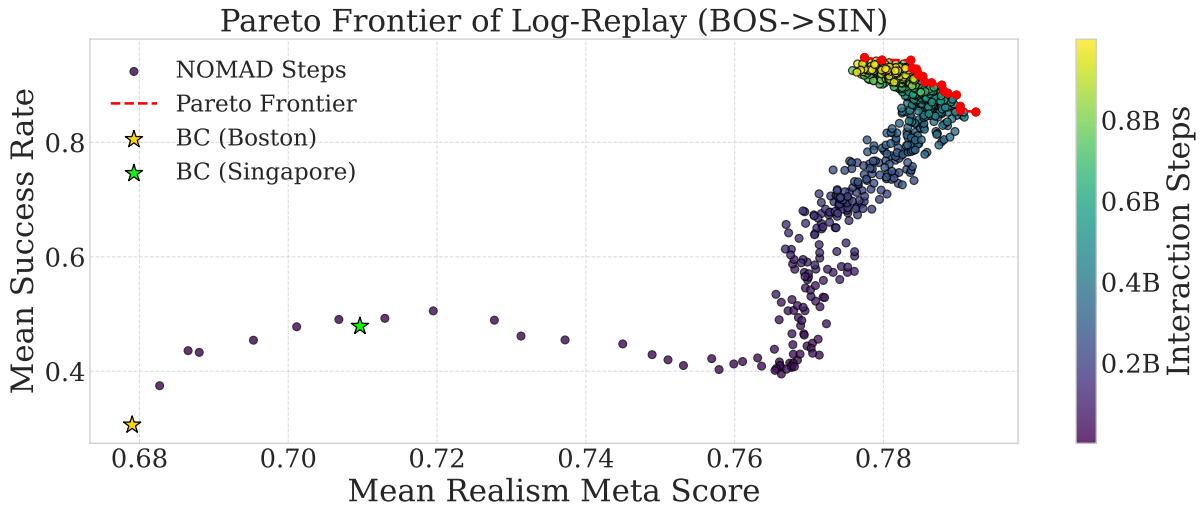


Figure 19. Pareto frontier of success rate versus realism meta score across training checkpoints for Singapore with log-replay sim agents. Each point corresponds to a policy checkpoint, colored by the number of interaction steps. The yellow star denotes the zero-shot transfer policy π^0 from Boston, while the lime star shows behavior cloning using Singapore trajectories. The red dashed line and points indicate the empirical Pareto frontier on this test set. Frontier checkpoints consistently dominate the baselines and exhibit only a mild trade-off between task success and realism.

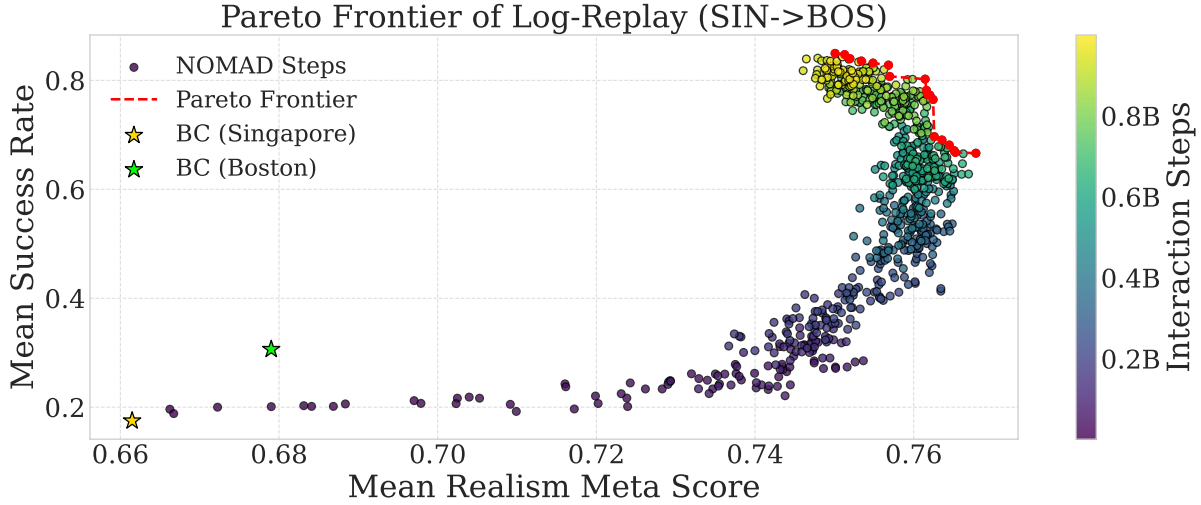


Figure 20. Pareto frontier of success rate versus realism meta score across training checkpoints for Boston with log-replay sim agents. Each point corresponds to a policy checkpoint, colored by the number of interaction steps. The yellow star denotes the zero-shot transfer policy π^0 from Singapore, while the lime star shows behavior cloning using Boston trajectories. The red dashed line and points indicate the empirical Pareto frontier on this test set. Frontier checkpoints consistently dominate the baselines and exhibit only a mild trade-off between task success and realism.

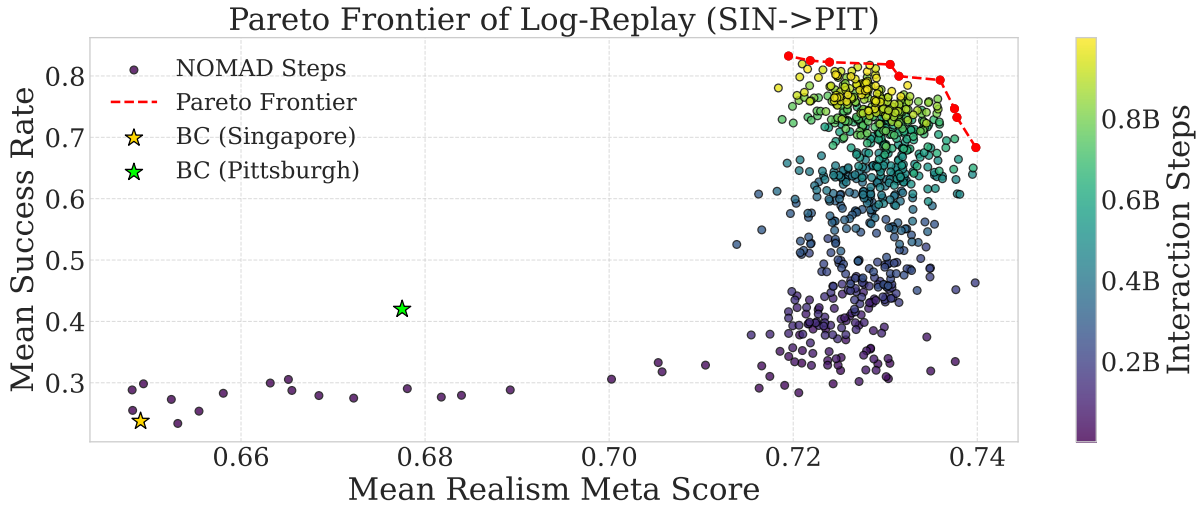


Figure 21. Pareto frontier of success rate versus realism meta score across training checkpoints for Pittsburgh with log-replay sim agents. Each point corresponds to a policy checkpoint, colored by the number of interaction steps. The yellow star denotes the zero-shot transfer policy π^0 from Singapore, while the lime star shows behavior cloning using Pittsburgh trajectories. The red dashed line and points indicate the empirical Pareto frontier on this test set. Frontier checkpoints consistently dominate the baselines and exhibit only a mild trade-off between task success and realism.

I.2. Cross-Play: Convention Consistency Across Independently Trained Agents

A common concern with multi-agent self-play is that independently trained agents may converge to seed-specific conventions that work well only when paired with themselves, but fail under *cross-play* with a novel partner (Hu et al., 2020). To test this, for each city-transfer setting we select $n = 5$ independent instances (different random seeds) for each checkpoint on the empirical success–realism Pareto frontier. We then evaluate all n^2 pairings, where diagonal entries correspond to *self-play* (same seed paired with itself) and off-diagonal entries correspond to *cross-play* (different seeds paired together).

Across all evaluated city pairs and frontier checkpoints, cross-play performance closely matches self-play. Figures 22–27 visualize this by plotting the 5×5 cross-play matrices for each frontier checkpoint; we observe no systematic degradation in off-diagonal entries. Tables 9–11 further summarize the results, showing that cross-play success and realism meta score remain within the variability observed under self-play at the same checkpoint. Overall, these results suggest NOMAD does not rely on fragile, seed-specific coordination conventions.

We attribute this stability to the strong behavioral priors and regularization used during adaptation: initializing from a pretrained behavior cloning policy and regularizing updates with KL regularization anchor learning to a shared, human-like driving mode, reducing the chance of divergent conventions across seeds.

Table 9. Self-play vs cross-play summary at Pareto-frontier checkpoints (Boston→Singapore). We evaluate each selected frontier checkpoint under both self-play (paired with the same-seed partner) and cross-play (paired with different-seed partners) using $n = 5$ independently trained seeds. We report mean \pm standard deviation across pairings. Cross-play success and realism closely match self-play at the same checkpoint, indicating that NOMAD does not rely on seed-specific conventions.

Checkpoint	Realism Self-Play	Realism Cross-Play	Success Rate Self-Play	Success Rate Cross-Play
3690	0.768 ± 0.004	0.769 ± 0.003	0.885 ± 0.011	0.885 ± 0.008
3710	0.771 ± 0.003	0.771 ± 0.003	0.873 ± 0.011	0.872 ± 0.010
3740	0.770 ± 0.003	0.769 ± 0.002	0.879 ± 0.017	0.880 ± 0.011
3930	0.768 ± 0.003	0.767 ± 0.002	0.897 ± 0.015	0.894 ± 0.013
3980	0.766 ± 0.004	0.766 ± 0.003	0.900 ± 0.014	0.902 ± 0.010
4010	0.766 ± 0.005	0.766 ± 0.003	0.901 ± 0.011	0.899 ± 0.009
4300	0.768 ± 0.003	0.768 ± 0.002	0.889 ± 0.012	0.888 ± 0.011
4610	0.767 ± 0.004	0.766 ± 0.002	0.899 ± 0.016	0.898 ± 0.011
4670	0.766 ± 0.002	0.765 ± 0.002	0.909 ± 0.016	0.907 ± 0.012
4700	0.766 ± 0.005	0.765 ± 0.003	0.902 ± 0.012	0.903 ± 0.010
4800	0.764 ± 0.002	0.763 ± 0.002	0.927 ± 0.013	0.927 ± 0.010
5000	0.765 ± 0.003	0.765 ± 0.003	0.917 ± 0.009	0.917 ± 0.008
6040	0.763 ± 0.001	0.763 ± 0.001	0.933 ± 0.005	0.934 ± 0.005
6150	0.765 ± 0.001	0.765 ± 0.001	0.919 ± 0.017	0.921 ± 0.010
6160	0.766 ± 0.004	0.766 ± 0.003	0.910 ± 0.013	0.910 ± 0.011
6570	0.765 ± 0.004	0.764 ± 0.003	0.926 ± 0.007	0.924 ± 0.005
7400	0.758 ± 0.003	0.758 ± 0.002	0.943 ± 0.011	0.943 ± 0.008
7480	0.763 ± 0.003	0.764 ± 0.002	0.930 ± 0.009	0.930 ± 0.007
7490	0.762 ± 0.002	0.763 ± 0.001	0.939 ± 0.004	0.939 ± 0.004

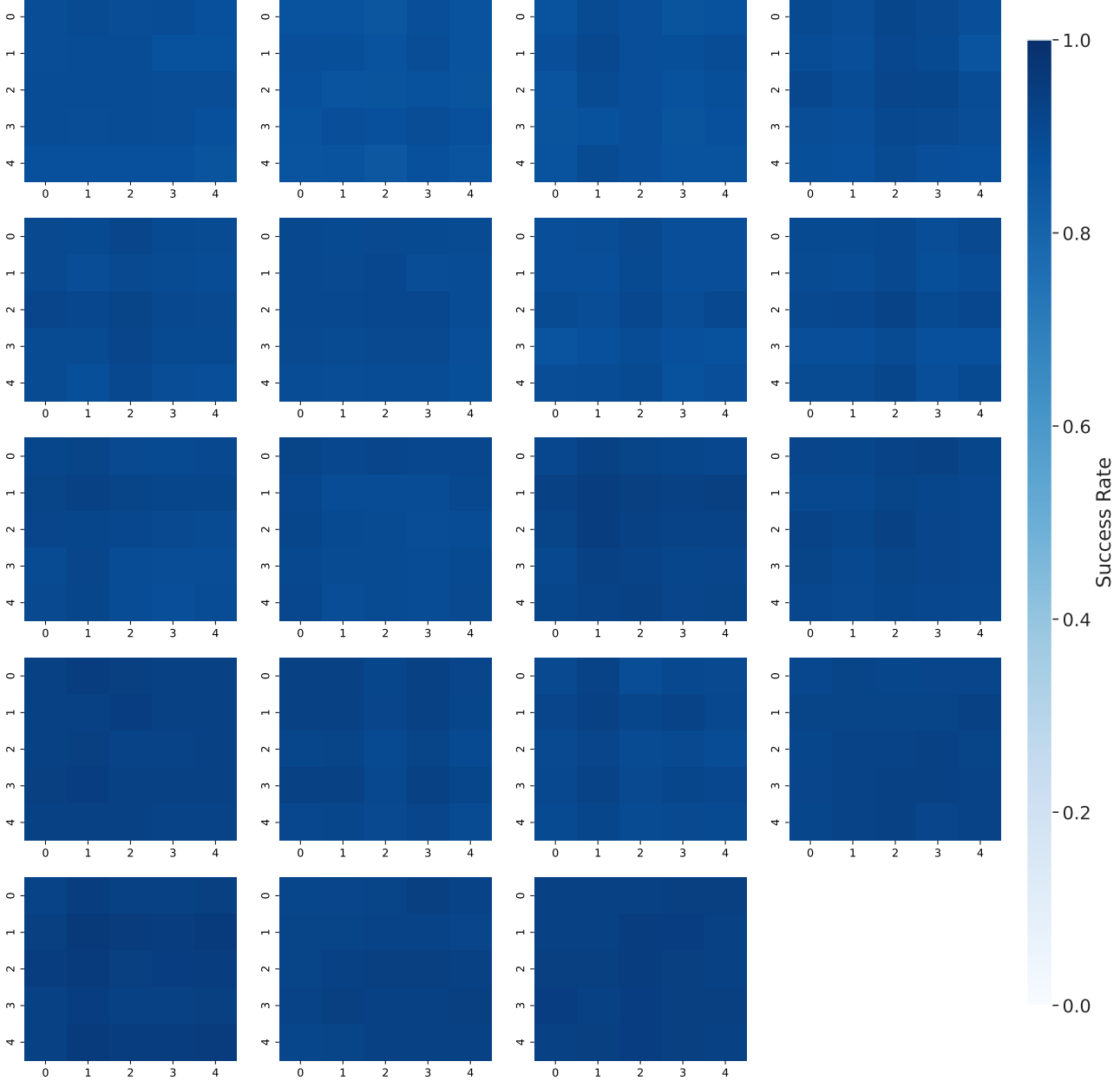


Figure 22. Cross-play success matrices across Pareto-frontier checkpoints (Boston→Singapore). Each panel corresponds to one selected checkpoint on the success-realism Pareto frontier. Within each panel, entry (i, j) reports the ego success rate when pairing seed i with seed j ($n = 5$ total seeds). Diagonal entries are self-play (same seed paired with itself), while off-diagonals are cross-play (different seeds). Off-diagonal performance is comparable to diagonal performance across checkpoints, indicating minimal sensitivity to partner seed.

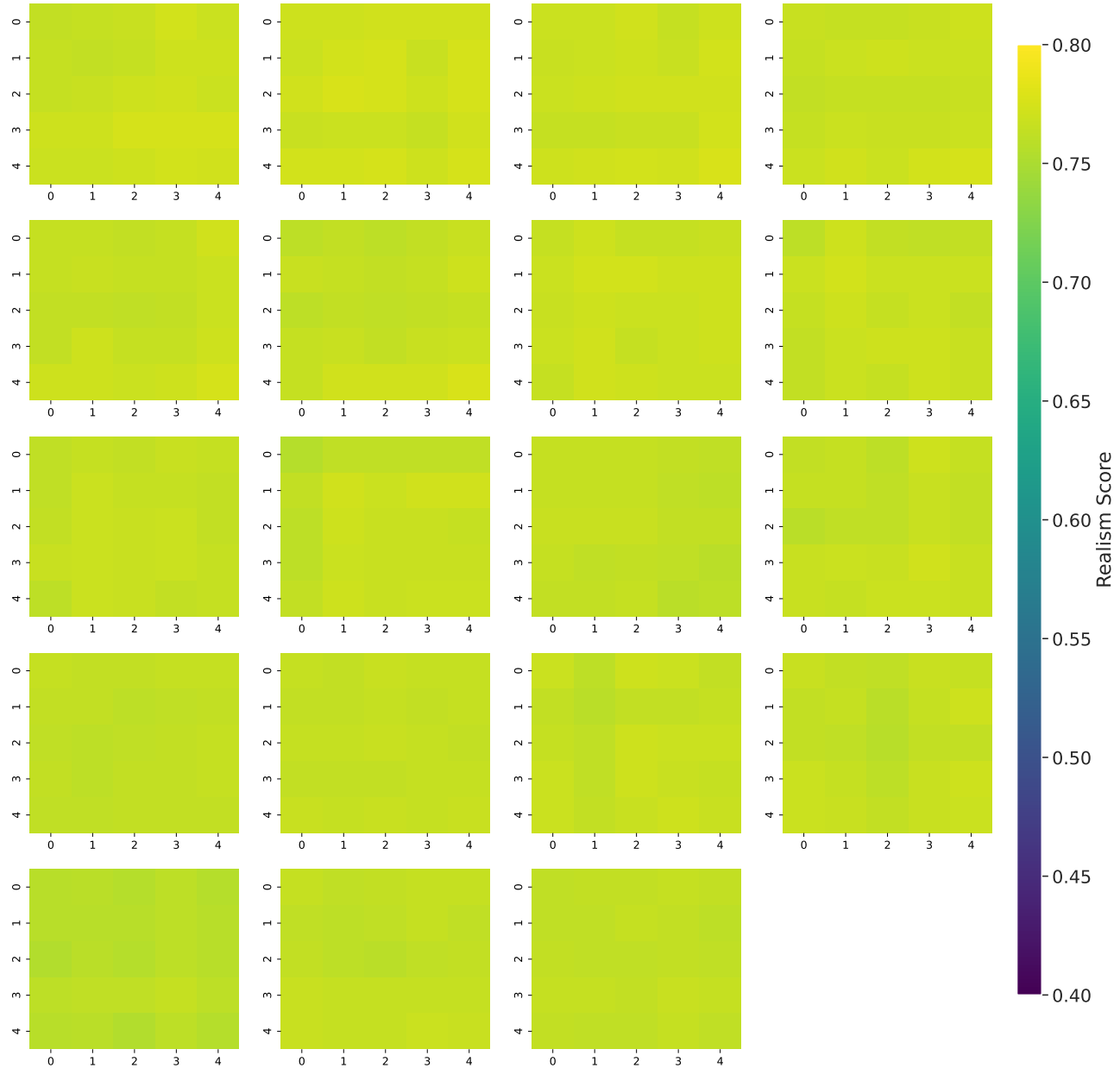


Figure 23. Cross-play realism matrices across Pareto-frontier checkpoints (Boston→Singapore). Each panel corresponds to one selected checkpoint on the success-realism Pareto frontier. Within each panel, entry (i, j) reports the ego realism meta score when pairing seed i with seed j ($n = 5$ total seeds). Diagonal entries are self-play (same seed paired with itself), while off-diagonals are cross-play (different seeds). Off-diagonal performance is comparable to diagonal performance across checkpoints, indicating minimal sensitivity to partner seed.

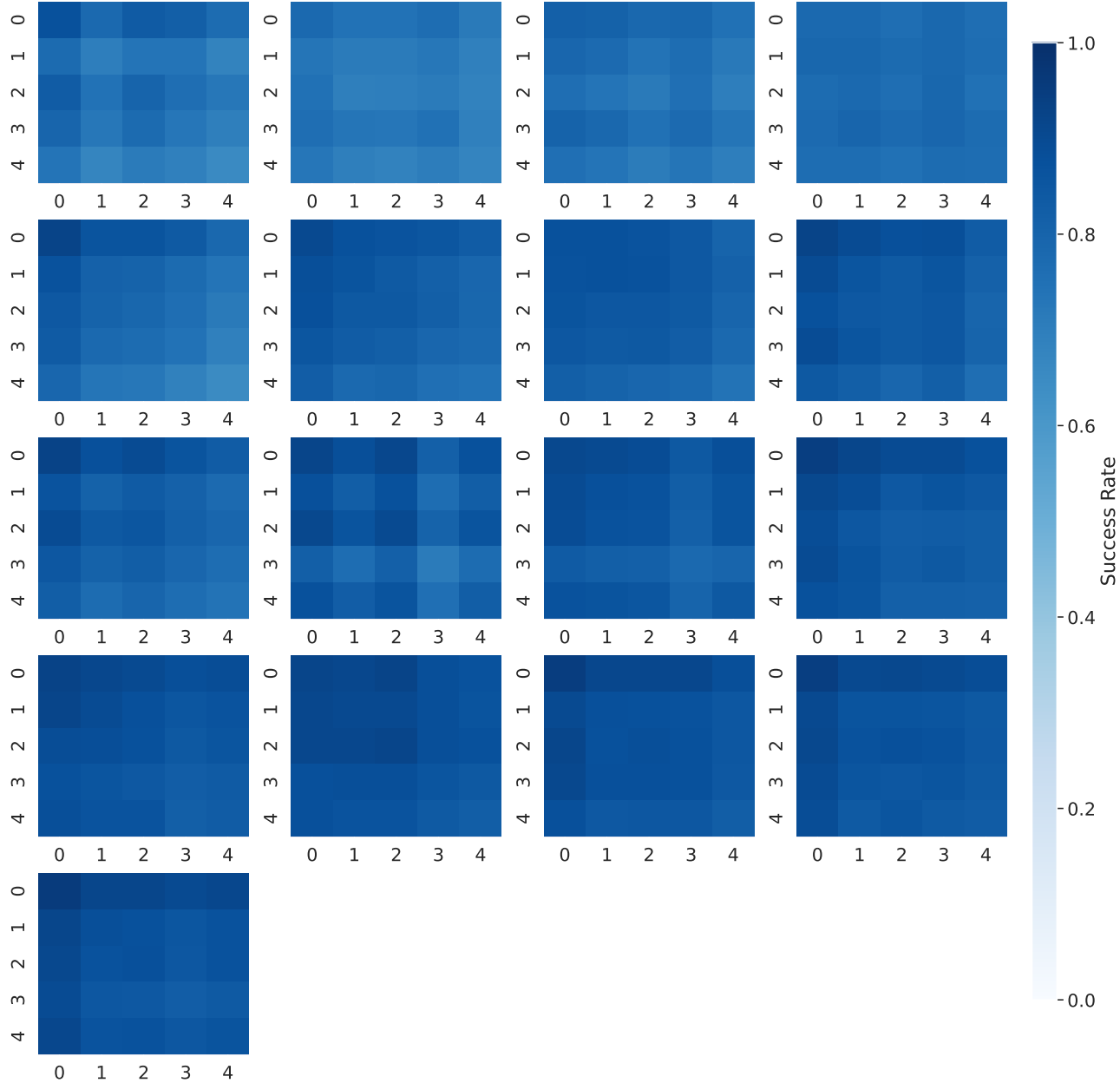


Figure 24. Cross-play success matrices across Pareto-frontier checkpoints (Singapore→Boston). Each panel corresponds to one selected checkpoint on the success-realism Pareto frontier. Within each panel, entry (i, j) reports the ego success rate when pairing seed i with seed j ($n = 5$ total seeds). Diagonal entries are self-play (same seed paired with itself), while off-diagonals are cross-play (different seeds). Off-diagonal performance is comparable to diagonal performance across checkpoints, indicating minimal sensitivity to partner seed.

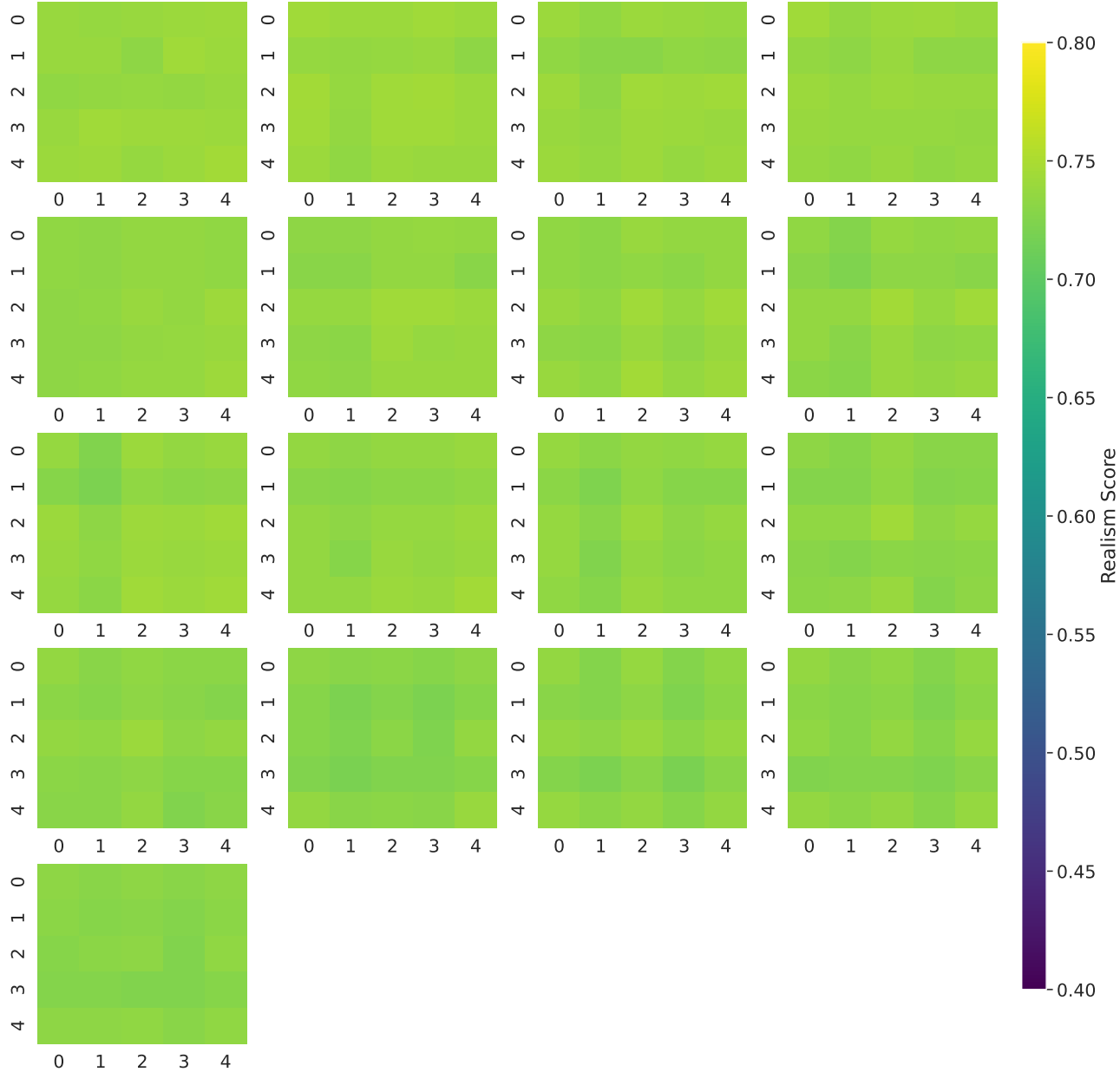


Figure 25. Cross-play realism matrices across Pareto-frontier checkpoints (Singapore→Boston). Each panel corresponds to one selected checkpoint on the success-realism Pareto frontier. Within each panel, entry (i, j) reports the ego realism meta score when pairing seed i with seed j ($n = 5$ total seeds). Diagonal entries are self-play (same seed paired with itself), while off-diagonals are cross-play (different seeds). Off-diagonal performance is comparable to diagonal performance across checkpoints, indicating minimal sensitivity to partner seed.

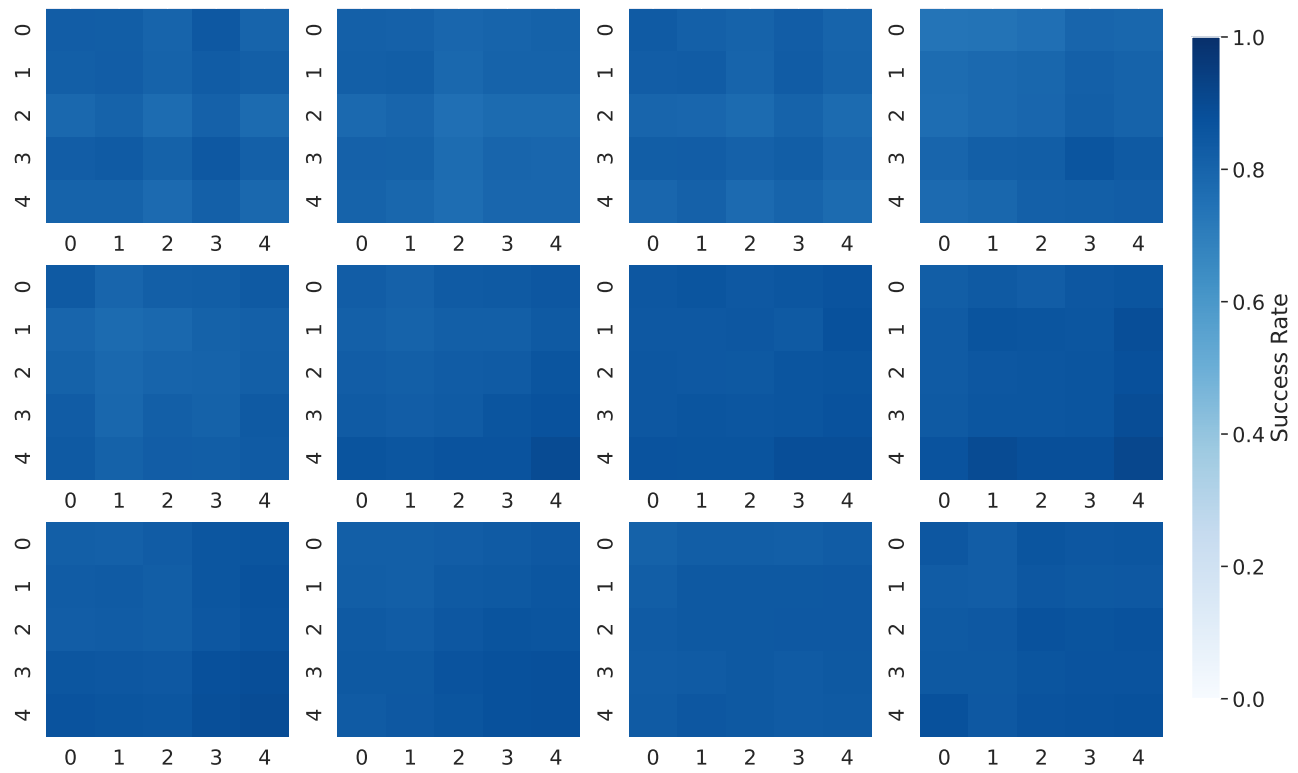


Figure 26. Cross-play success matrices across Pareto-frontier checkpoints (Singapore→Pittsburgh). Each panel corresponds to one selected checkpoint on the success-realism Pareto frontier. Within each panel, entry (i, j) reports the ego success rate when pairing seed i with seed j ($n = 5$ total seeds). Diagonal entries are self-play (same seed paired with itself), while off-diagonals are cross-play (different seeds). Off-diagonal performance is comparable to diagonal performance across checkpoints, indicating minimal sensitivity to partner seed.

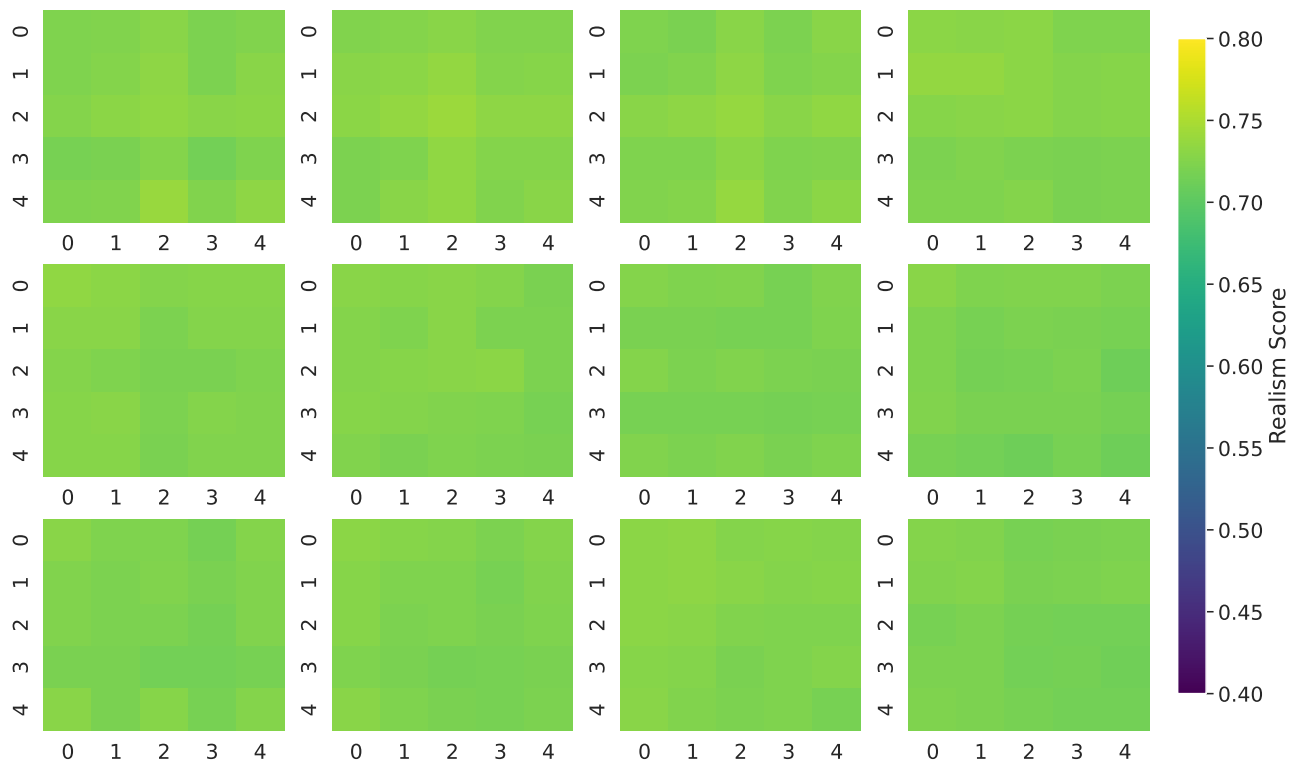


Figure 27. Cross-play realism matrices across Pareto-frontier checkpoints (Singapore→Pittsburgh). Each panel corresponds to one selected checkpoint on the success–realism Pareto frontier. Within each panel, entry (i, j) reports the ego realism meta score when pairing seed i with seed j ($n = 5$ total seeds). Diagonal entries are self-play (same seed paired with itself), while off-diagonals are cross-play (different seeds). Off-diagonal performance is comparable to diagonal performance across checkpoints, indicating minimal sensitivity to partner seed.

Table 10. Self-play vs cross-play summary at Pareto-frontier checkpoints (Singapore→Boston). We evaluate each selected frontier checkpoint under both self-play (paired with the same-seed partner) and cross-play (paired with different-seed partners) using $n = 5$ independently trained seeds. We report mean \pm standard deviation across pairings. Cross-play success and realism closely match self-play at the same checkpoint, indicating that NOMAD does not rely on seed-specific conventions.

Checkpoint	Realism Self-Play	Realism Cross-Play	Success Rate Self-Play	Success Rate Cross-Play
4860	0.740 ± 0.003	0.738 ± 0.003	0.751 ± 0.077	0.749 ± 0.046
4910	0.740 ± 0.003	0.739 ± 0.003	0.724 ± 0.036	0.721 ± 0.023
4920	0.738 ± 0.004	0.737 ± 0.004	0.756 ± 0.042	0.755 ± 0.029
4940	0.738 ± 0.004	0.737 ± 0.002	0.776 ± 0.012	0.771 ± 0.012
6180	0.737 ± 0.003	0.735 ± 0.002	0.783 ± 0.089	0.783 ± 0.055
6240	0.736 ± 0.005	0.735 ± 0.004	0.828 ± 0.056	0.825 ± 0.035
6250	0.736 ± 0.005	0.736 ± 0.004	0.832 ± 0.050	0.832 ± 0.031
6290	0.735 ± 0.007	0.733 ± 0.004	0.846 ± 0.053	0.845 ± 0.033
6310	0.736 ± 0.008	0.736 ± 0.005	0.824 ± 0.063	0.824 ± 0.040
6370	0.736 ± 0.005	0.735 ± 0.004	0.836 ± 0.072	0.836 ± 0.048
6800	0.733 ± 0.006	0.733 ± 0.004	0.854 ± 0.043	0.852 ± 0.032
6840	0.732 ± 0.006	0.731 ± 0.004	0.862 ± 0.048	0.860 ± 0.031
6880	0.732 ± 0.005	0.731 ± 0.003	0.870 ± 0.039	0.870 ± 0.025
7040	0.729 ± 0.006	0.727 ± 0.004	0.885 ± 0.039	0.882 ± 0.023
7520	0.731 ± 0.007	0.730 ± 0.004	0.880 ± 0.040	0.878 ± 0.024
7530	0.731 ± 0.006	0.730 ± 0.004	0.873 ± 0.038	0.871 ± 0.025
7540	0.730 ± 0.004	0.729 ± 0.003	0.881 ± 0.042	0.879 ± 0.027

Table 11. Self-play vs cross-play summary at Pareto-frontier checkpoints (Singapore→Pittsburgh). We evaluate each selected frontier checkpoint under both self-play (paired with the same-seed partner) and cross-play (paired with different-seed partners) using $n = 5$ independently trained seeds. We report mean \pm standard deviation across pairings. Cross-play success and realism closely match self-play at the same checkpoint, indicating that NOMAD does not rely on seed-specific conventions.

Checkpoint	Realism Self-Play	Realism Cross-Play	Success Rate Self-Play	Success Rate Cross-Play
6030	0.726 ± 0.007	0.726 ± 0.005	0.809 ± 0.029	0.809 ± 0.018
6040	0.730 ± 0.005	0.728 ± 0.005	0.796 ± 0.024	0.793 ± 0.015
6080	0.727 ± 0.006	0.727 ± 0.005	0.806 ± 0.029	0.804 ± 0.016
6340	0.728 ± 0.006	0.726 ± 0.004	0.798 ± 0.041	0.794 ± 0.024
6550	0.727 ± 0.005	0.725 ± 0.003	0.809 ± 0.025	0.812 ± 0.017
7010	0.725 ± 0.004	0.724 ± 0.004	0.843 ± 0.031	0.838 ± 0.018
7020	0.721 ± 0.003	0.721 ± 0.003	0.855 ± 0.016	0.857 ± 0.011
7050	0.719 ± 0.006	0.720 ± 0.004	0.862 ± 0.030	0.858 ± 0.020
7070	0.722 ± 0.005	0.722 ± 0.004	0.849 ± 0.031	0.849 ± 0.018
7370	0.723 ± 0.004	0.723 ± 0.004	0.847 ± 0.027	0.845 ± 0.015
7470	0.726 ± 0.005	0.726 ± 0.003	0.832 ± 0.014	0.836 ± 0.009
7520	0.720 ± 0.005	0.719 ± 0.003	0.856 ± 0.017	0.852 ± 0.013

J. Effect of Map Mirroring for Opposite-Side Driving

A natural question in cross-city transfer is whether a policy trained in a right-hand driving city can be adapted to a left-hand driving city by simply mirroring the source-city map. Such a geometric transformation would, in principle, align the driving-side convention between cities such as Boston and Singapore, without requiring additional training.

To evaluate this hypothesis, we mirror the Singapore map and evaluate zero-shot transfer policies on the mirrored map. Examples of scenarios after mirroring are provided in Figure 8, and quantitative results are summarized in Table 12. Here, BOS and SIN denote scenarios from Boston and Singapore, respectively. π_{BOS}^0 and π_{SIN}^0 denote BC policies trained in Boston (right-hand traffic) and Singapore (left-hand traffic), respectively.

The results show that map mirroring yields only marginal improvements in zero-shot performance. While mirroring partially addresses the left-hand versus right-hand driving mismatch, the resulting gains are small relative to those achieved by self-play fine-tuning. This indicates that cross-city performance degradation cannot be attributed solely to driving-side conventions. Importantly, this experiment isolates the effect of geometric alignment while holding the policy fixed. The limited benefit of mirroring suggests that cross-city distribution shift arises from deeper factors, including differences in road geometry, intersection topology, lane-width distributions, and traffic density patterns. These interaction-level and structural differences cannot be resolved through geometric transformations alone, motivating the need for adaptive interaction-aware learning as enabled by NOMAD.

Table 12. Effect of map mirroring on zero-shot cross-city transfer. BOS and SIN denote Boston and Singapore scenarios. π_{BOS}^0 and π_{SIN}^0 denote behavior cloning policies trained in Boston and Singapore. Mirroring the city map yields only modest performance improvements, indicating that cross-city distribution shift extends beyond driving-side conventions and cannot be resolved by geometric transformations alone.

Policy	Scenarios	Realism Meta Score	Success Rate
π_{BOS}^0	Original BOS	0.7022	55.77%
	Original SIN	0.6795	42.25%
	Mirrored SIN	0.6756	43.96%
π_{SIN}^0	Original SIN	0.7011	55.49%
	Original BOS	0.6585	36.67%
	Mirrored BOS	0.6278	38.20%

K. Additional Hold-Out Evaluation of Selected Frontier Checkpoints

To assess potential selection bias, particularly overestimation when constructing the empirical Pareto frontier from a finite evaluation set, we additionally evaluate the checkpoints selected on the frontier using an extra held-out set of 800 scenarios (new test set) that is disjoint from both training and the original test set. Ideally, both evaluation sets are i.i.d. samples from the same underlying scenario distribution and that metrics are noise-free, the re-evaluated frontier checkpoints would be expected to remain close to, and typically slightly below, the frontier estimated on the original test set.

Figure 28, Figure 29, and Figure 30 show the evaluation results with blue triangles in Boston–Singapore, Singapore–Boston, Singapore–Pittsburgh transfers, respectively. For the success rate, the evaluation results on the new test set closely aligned with the results on the original test set, showing that there is little bias along our empirical Pareto frontier. In contrast, along the realism axis, we observe that re-evaluated points can deviate slightly from our expectation and occasionally appear right to the original frontier, specifically for Boston–Singapore and Singapore–Pittsburgh transfers. A possible reason is that WOSAC realism is computed relative to the set’s ground-truth trajectories; hence small differences in the composition of scenarios or expert driving style in the held-out set can lead to systematic shifts in the absolute realism meta score even when success rates remain similar. To verify this argument, we checked the WOSAC realism meta score of human trajectories in different sets of scenarios from Singapore, which is the upper bound to their corresponding set, showing in Table 13.

Table 13. The WOSAC realism meta scores of human trajectories in different sets of scenarios.

Dataset	Value
Test set@Singapore	0.8581
New test set@Singapore	0.8602
Test set@Boston	0.8311
New test set@Boston	0.8284
Test set@Pittsburgh	0.8339
New test set@Pittsburgh	0.8392

The results demonstrate the quantitative difference in the realism meta score between different datasets even within one city, which explain the outward shift of re-evaluated points. Considering this difference, we present that is not severe overestimation of our frontier checkpoint selection.

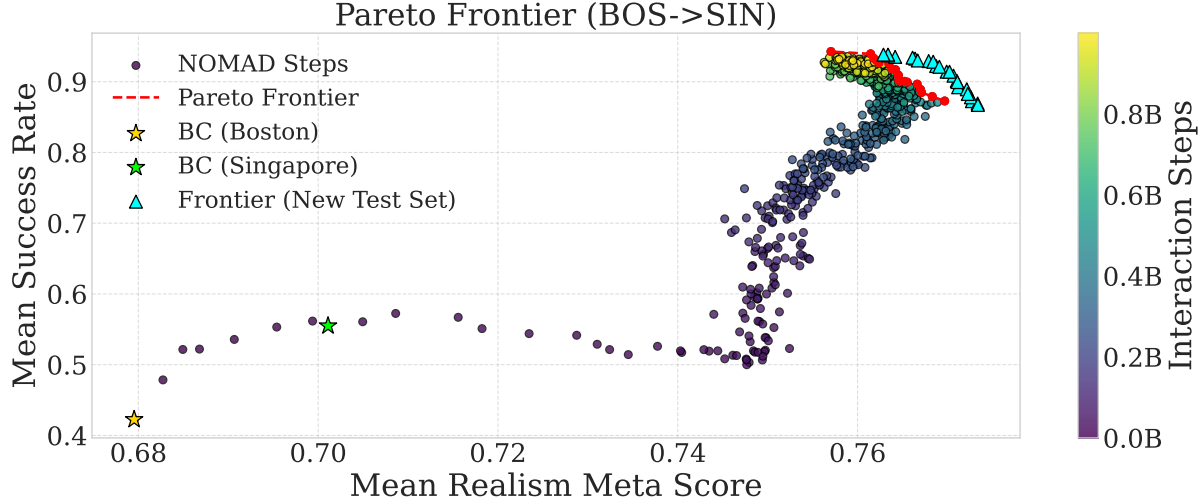


Figure 28. Pareto frontier of success rate versus realism meta score across training checkpoints under Boston-to-Singapore transfer. Each point corresponds to a policy checkpoint, colored by the number of interaction steps. The yellow star denotes the zero-shot transfer policy π^0 from Boston, while the lime star shows behavior cloning using Singapore trajectories. The red dashed line and points indicate the empirical Pareto frontier on this test set. Frontier checkpoints consistently dominate the baselines and exhibit only a mild trade-off between task success and realism. Blue triangles report the performance of selected frontier policies on a held-out Singapore test set, confirming that the Pareto dominance generalizes beyond the test data.

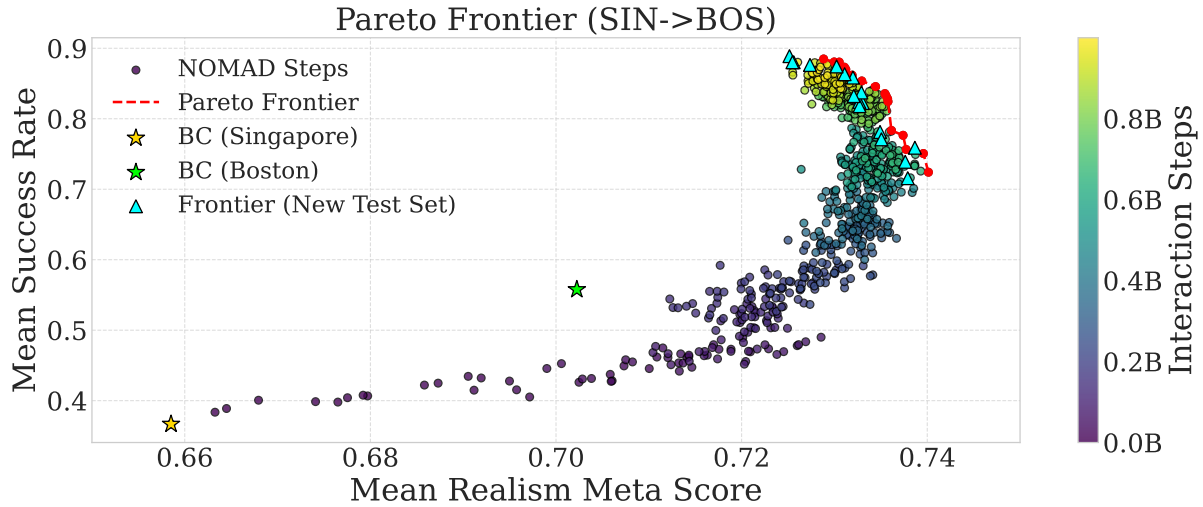


Figure 29. Pareto frontier of success rate versus realism meta score across training checkpoints under Singapore-to-Boston transfer. Each point corresponds to a policy checkpoint, colored by the number of interaction steps. The yellow star denotes the zero-shot transfer policy π^0 from Singapore, while the lime star shows behavior cloning using Boston trajectories. The red dashed line and points indicate the empirical Pareto frontier on this test set. Frontier checkpoints consistently dominate the baselines and exhibit only a mild trade-off between task success and realism. Blue triangles report the performance of selected frontier policies on a held-out Boston test set, confirming that the Pareto dominance generalizes beyond the test data.

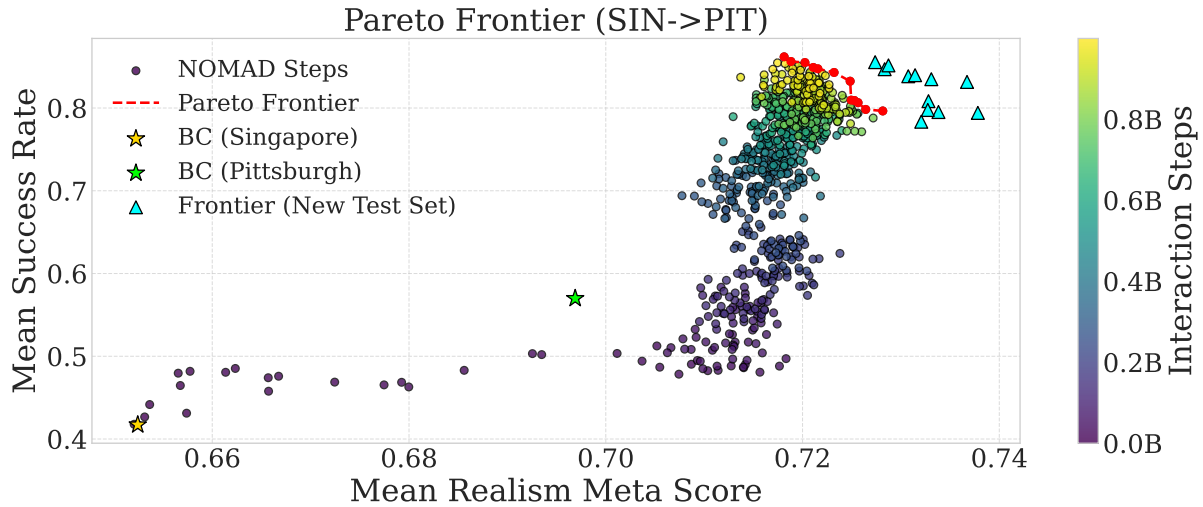


Figure 30. Pareto frontier of success rate versus realism meta score across training checkpoints under Singapore-to-Pittsburgh transfer. Each point corresponds to a policy checkpoint, colored by the number of interaction steps. The yellow star denotes the zero-shot transfer policy π^0 from Singapore, while the lime star shows behavior cloning using Boston trajectories. The red dashed line and points indicate the empirical Pareto frontier on this test set. Frontier checkpoints consistently dominate the baselines and exhibit only a mild trade-off between task success and realism. Blue triangles report the performance of selected frontier policies on a held-out Pittsburgh test set, confirming that the Pareto dominance generalizes beyond the test data.

L. Qualitative results

We provide extensive qualitative results in the form of representative frames of rendered videos to complement the quantitative evaluations in the main paper. The visualizations focus on bidirectional city transfer between Boston and Singapore, comparing zero-shot transferred policies with policies adapted by NOMAD (we chose one checkpoint on the frontier for each city) under identical initial conditions. These examples highlight characteristic failure modes induced by cross-city distribution shifts and illustrate how map-based self-play enables robust adaptation to target-city geometry and interaction patterns.

Across both transfer directions, zero-shot policies exhibit several recurring failure patterns. First, geometric mismatches (Figure 31), such as narrower lane widths in Singapore, lead to unstable lane-keeping and off-road behavior when transferring from Boston. Second, systematic driving-side biases appear in both directions (Figure 32 and Figure 33): policies trained in right-hand traffic tend to violate lane conventions in Singapore, while policies trained in left-hand traffic exhibit analogous failures in Boston, resulting in collisions and off-road events. Third, sequential decision errors under closed-loop execution arise in cluttered environments with static obstacles (Figure 34), where zero-shot policies make inappropriate avoidance choices at successive decision points, causing cascading collisions. Finally, interaction-level mismatches are observed in multi-vehicle scenarios (Figure 35), including miscalibrated speed regulation and incorrect yielding behavior at intersections, leading to unsafe interactions among moving agents.

In contrast, NOMAD consistently mitigates these failure modes across both transfer directions. By leveraging map-based self-play in a target-city simulator, NOMAD adapts its lane-keeping behavior to local road geometry, corrects driving-side biases, selects more appropriate avoidance and corrective actions in cluttered environments, and exhibits improved speed control and yielding behavior in multi-agent interactions. Together, these qualitative results reinforce the quantitative findings, demonstrating the efficacy of map-based self-play adaptation to the target city.

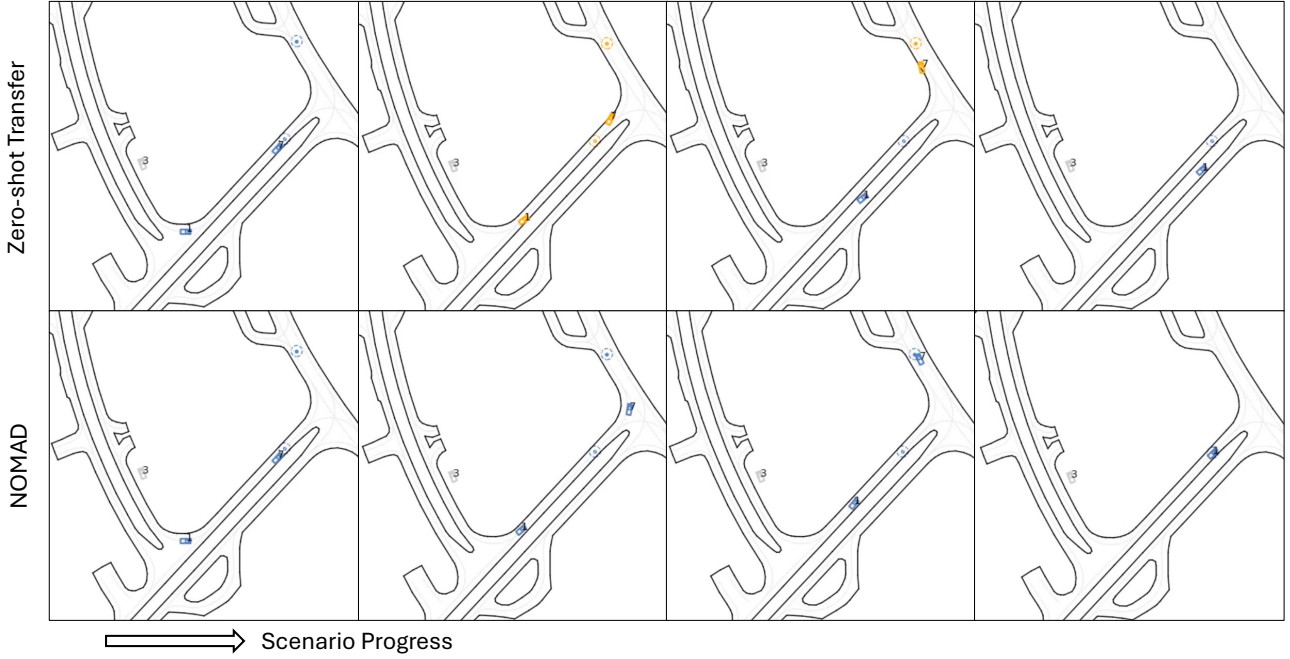


Figure 31. Narrow-lane failure under Boston-to-Singapore transfer. Representative frames from a Boston-to-Singapore transfer scenario illustrating geometric mismatch in narrow roads. Top: zero-shot transferred policy. Bottom: NOMAD-adapted policy. The zero-shot policy, trained in Boston, fails to account for the narrower lane geometry commonly found in Singapore and gradually drifts outside the drivable region, resulting in off-road behavior (yellow). In contrast, NOMAD adapts to the target-city road geometry through map-based self-play and maintains stable lane-centering throughout the maneuver. Blue denotes the controlled vehicle, the white circle indicates the goal location, white boxes represent static vehicles, and yellow highlights collision with road boundaries.

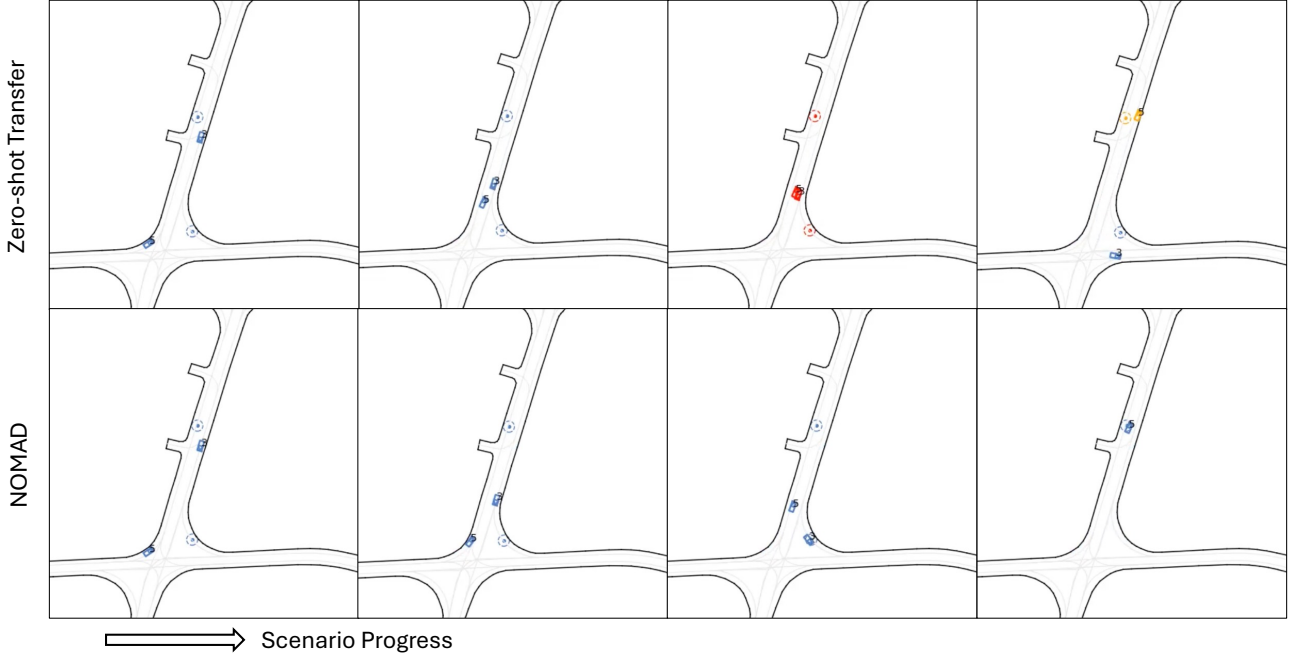


Figure 32. Driving-side mismatch under Boston-to-Singapore transfer. Top: zero-shot transferred policy. Bottom: NOMAD-adapted policy. The zero-shot policy exhibits a systematic bias toward right-hand driving learned in the source city, leading to lane violation and collision in the left-hand traffic setting of Singapore. In contrast, NOMAD adapts its lane-keeping behavior through map-based self-play and consistently drives on the correct side of the road. Blue denotes the controlled vehicle, the circle indicates the goal location, white boxes represent static vehicles, and red and yellow highlights collision with vehicles and road boundaries, respectively.

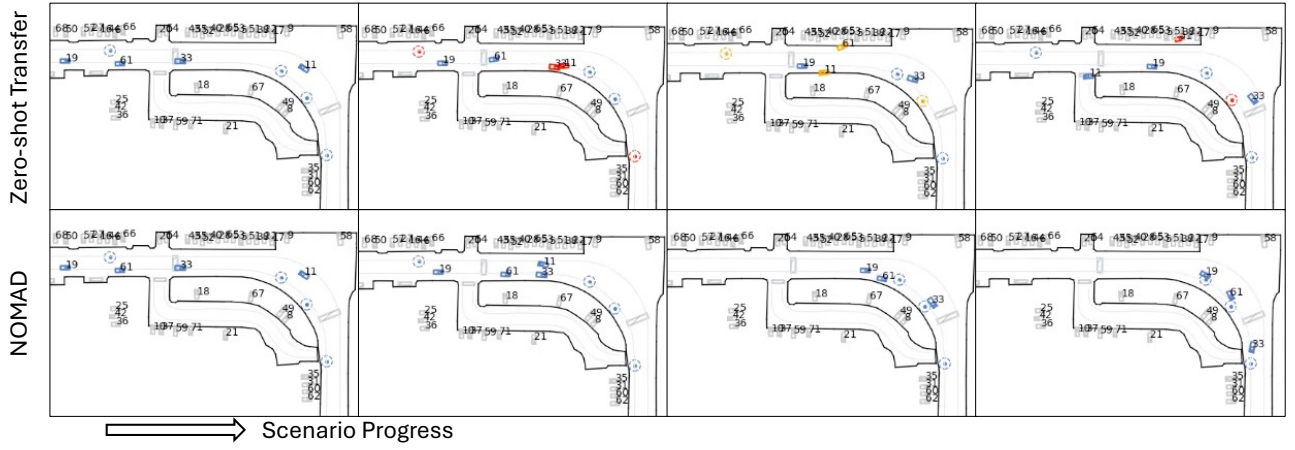


Figure 33. Driving-side mismatch under Singapore-to-Boston transfer. Top: zero-shot transferred policy. Bottom: NOMAD-adapted policy. The zero-shot policy retains a left-hand driving bias learned in the source city: vehicle 61 and vehicle 11 both tend to keep left, resulting in lane violations, collision, and off-road behavior in the right-hand traffic setting of Boston. In contrast, NOMAD adapts its lane-keeping behavior via map-based self-play and consistently drives on the correct side of the road. Blue denotes the controlled vehicle, the circle indicates the goal location, white boxes represent static vehicles, and red and yellow highlights collision with vehicles and road boundaries, respectively.

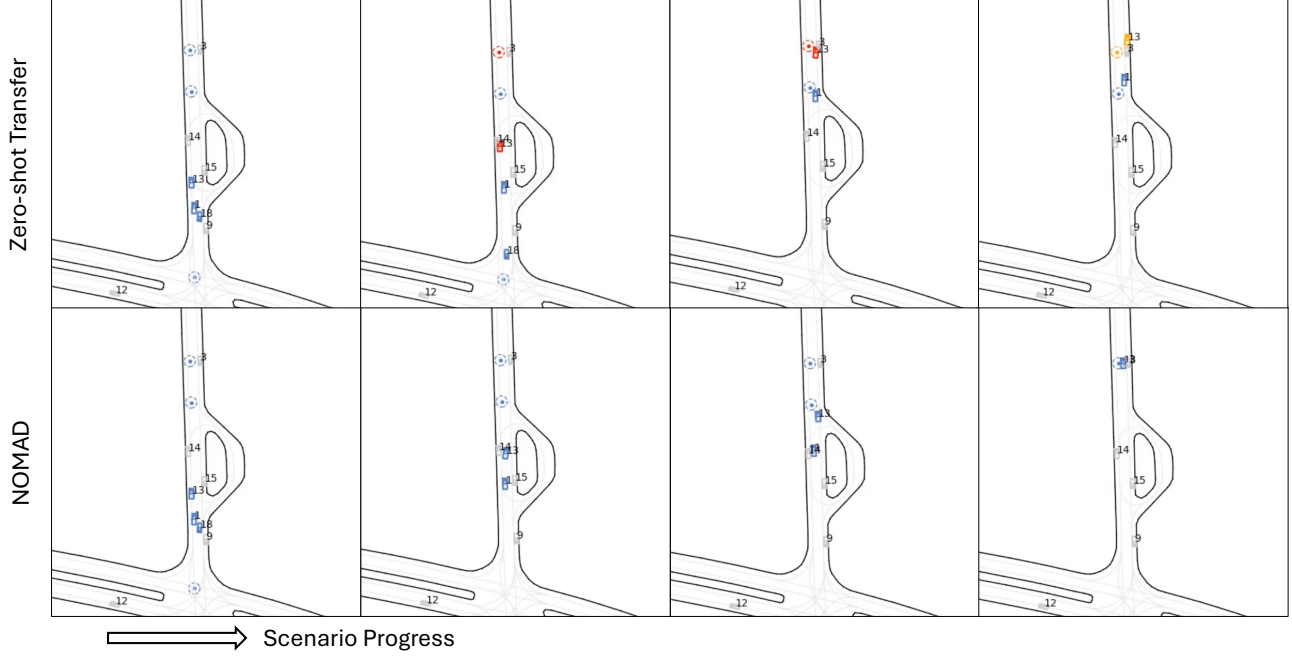


Figure 34. Cascading collision failure from a Boston-to-Singapore transfer scenario involving dense static obstacles. Top: zero-shot transferred policy. Bottom: NOMAD-adapted policy. The zero-shot policy fails to execute an early rightward avoidance maneuver and collides with the first static vehicle. Following the collision, it initiates a right-turn corrective action, whereas a leftward maneuver is required to avoid the second obstacle, leading to a cascading collision. In contrast, NOMAD selects appropriate avoidance actions at both decision points, illustrating improved closed-loop decision making under target-city geometric and obstacle-layout shifts. Blue denotes the controlled vehicle, the circle indicates the goal location, white boxes represent static vehicles, and red highlights collision with vehicles.

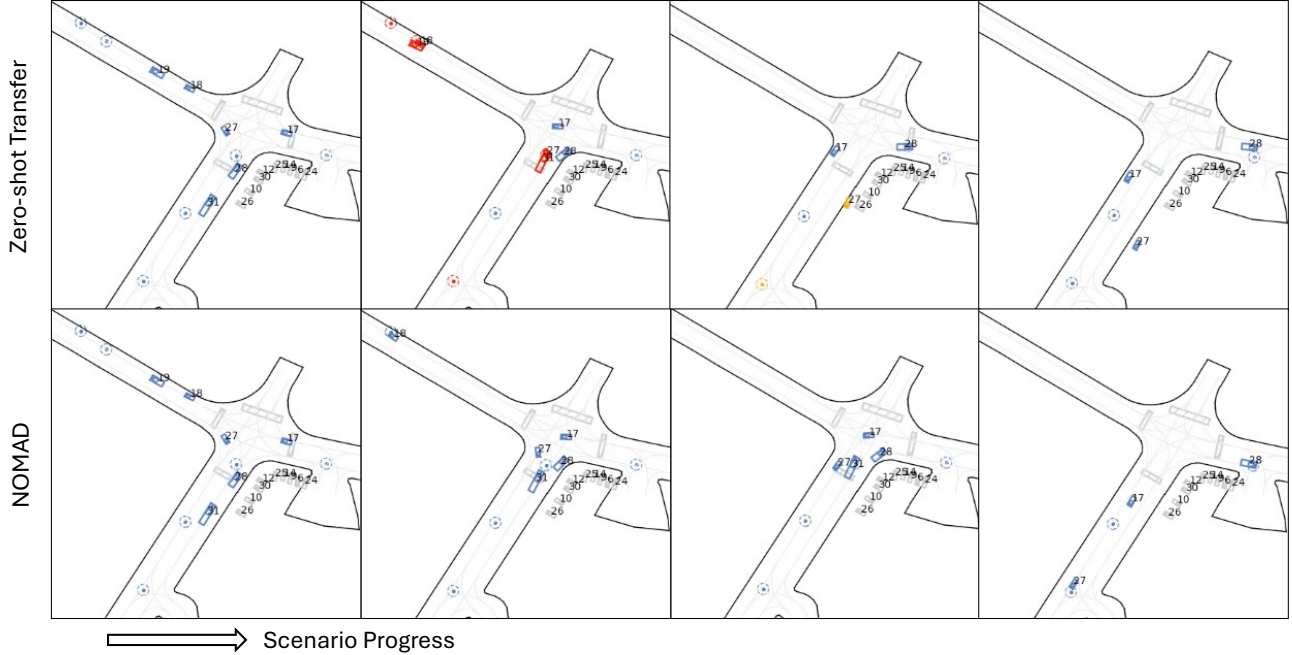


Figure 35. Interaction mismatch frames from a Singapore-to-Boston transfer scenario involving multiple interacting vehicles. Top: zero-shot transferred policy. Bottom: NOMAD-adapted policy. The zero-shot policy exhibits miscalibrated interaction behavior: vehicle 18 approaches significantly faster than vehicle 19, leading to a collision, while vehicle 27 fails to yield appropriately to vehicle 31 at the intersection. In contrast, NOMAD learns more balanced speed regulation and yielding behavior through map-based self-play, enabling safe and coordinated multi-vehicle interaction in the target city. Blue denotes the controlled vehicle, the circle indicates the goal location, white boxes represent static vehicles, and red and yellow highlights collision with vehicles and road boundaries, respectively.